Ocean Engineering 260 (2022) 112026

Contents lists available at ScienceDirect

Ocean Engineering

journal homepage: www.elsevier.com/locate/oceaneng

A three-dimensional fluid-structure interaction model based on SPH and lattice-spring method for simulating complex hydroelastic problems

K.C. Ng [a,*], W.C. Low [a], Hailong Chen [b], A. Tafuni [c], A. Nakayama [d]

[a] *Department of Mechanical, Materials and Manufacturing Engineering, University of Nottingham Malaysia, Jalan Broga, 43500, Semenyih, Selangor Darul Ehsan, Malaysia*
[b] *Department of Mechanical Engineering, University of Kentucky, Lexington, KY, 40513, USA*
[c] *School of Applied Engineering and Technology, New Jersey Institute of Technology, Newark, USA*
[d] *Faculty of Engineering and Green Technology, Universiti Tunku Abdul Rahman, Kampar, 31900, Perak, Malaysia*

ARTICLE INFO

Keywords:
Smoothed particle hydrodynamics (SPH)
Fluid structure interaction (FSI)
DualSPHysics
Volume compensated particle method (VCPM)
Lattice particle method (LPM)
Lattice spring model (LSM)

ABSTRACT

The present work revolves around the development of a 3D particle-based Fluid-Structure Interaction (FSI) solver to simulate hydroelastic problems that involve free surface. The three-dimensional Volume-Compensated Particle Method (VCPM) for modelling deformable solid bodies is developed within the open-source SPH software package DualSPHysics. Complex 3D FSI problems are readily simulated within a reasonable time frame thanks to the parallel scalability of DualSPHysics on both CPU and GPU. The Sequential Staggered (SS) scheme paired with a multiple time-stepping procedure is implemented in DualSPHysics for coupling the SPH and VCPM models. It is found that the SPH-VCPM method is computationally more efficient than the previously reported SPH-TLSPH method. Extensive validations have been performed based on some very recent 3D experimental setups that involve violent free surface and complex structural dynamics. Findings from this research highlight the capability of the 3D SPH-VCPM model to reproduce some of the physical observations that were not captured by previous 2D studies. Some preliminary 3D FSI results involving solid fracture are also demonstrated.

1. Introduction

Fluid Structure Interaction (FSI) is prevalent across many engineering disciplines such as coastal engineering (Danielsen et al., 2005), design of offshore structures for renewable energy (Chella et al., 2012; Wang et al., 2020), biomedical engineering (Ariane et al., 2017), marine engineering (Ming et al., 2018), and more. In general, it is very costly to perform experimental study on FSI problems. Fortunately, recent advancements in computing architecture and numerical schemes developed within the Computational Fluid Dynamics (CFD) and Computational Solid Mechanics (CSM) communities have enabled a more in-depth study of challenging problems involving FSI.

Conventionally, mesh-based methods such as Finite Element Method (FEM) and Finite Volume Method (FVM) are used for solid and fluid modeling, respectively. Although FEM offers high accuracy and stability, it faces difficulty in modeling problems with large deformations and it often requires special techniques such as local re-meshing in order to preserve the mesh quality. Similarly, for fluid modeling, it becomes more difficult for mesh-based methods (e.g. FVM) to simulate flow problems involving large fluid deformations arising at the free surface (e.g. breaking waves) and moving fluid-fluid and fluid-solid interfaces. In order to model free surfaces using mesh-based methods, numerical techniques such as Volume of Fluid (VOF) (Hirt and Nichols, 1981) and Level-Set (LS) (Sussman, 1994) are common strategies used to track the position of a free surface. While VOF and LS methods can be used to simulate non-breaking free surface flow effectively, it is computationally challenging to reconstruct the highly fragmented free surface (e.g. breaking wave) using VOF/LS on Eulerian meshes.

In view of this, particle method such as Smoothed Particle Hydrodynamics (SPH) has been developed to address the limitations of mesh-based methods. For fluid modeling, unlike VOF/LS in mesh-based methods, the inherent advantage of a SPH model such as the weakly-compressible SPH (WCSPH) in simulating hydro-elastic problems is its ability to model the free surface without the need of tracking. For solid modeling, SPH can handle large deformations; however, it suffers from numerical issues such as linear inconsistency (Liu and Liu, 2006), tensile instability (Swelge et al., 1995; Gray et al., 2001) and rank deficiency (Vignjevic et al., 2000). The linear inconsistency issue in the

* Corresponding author.
E-mail addresses: khaiching.ng@nottingham.edu.my, ngkhaiching2000@yahoo.com (K.C. Ng).

https://doi.org/10.1016/j.oceaneng.2022.112026
Received 14 March 2022; Received in revised form 27 June 2022; Accepted 14 July 2022
Available online 7 August 2022

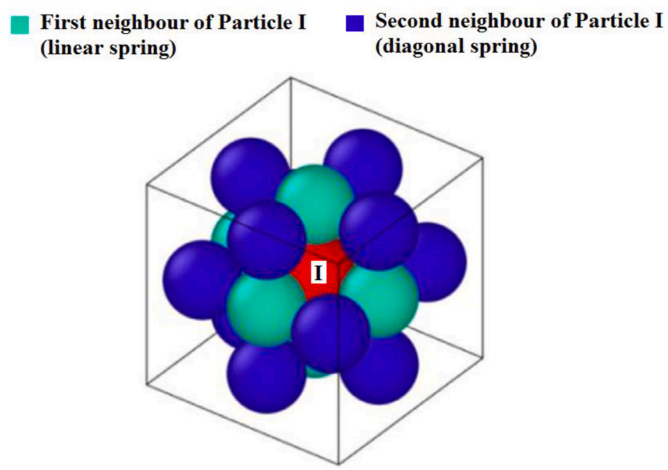

Fig. 1. The Simple Cubic (SC) lattice structure in 3D VCPM method (Chen and Liu, 2016). There are 18 neighbouring particles (6 first neighbours + 12 s neighbours) surrounding a solid particle I.

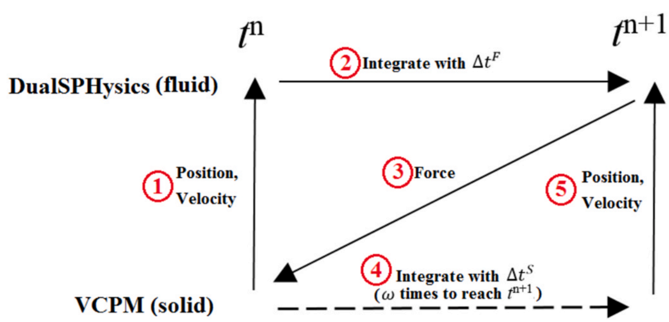

Fig. 2. Solution sequence of the present Sequential Staggered (SS) coupling scheme. Note that at step 4, the solid solver is integrated multiple (ω) times to synchronize with the fluid solver.

conventional SPH approximation can be resolved, for example, by using the kernel correction method (Bonet and Lok, 1999) and the corrective method based on Taylor series (Chen and Beraun, 2000). The Total Lagrangian SPH (TLSPH) formulation (Belytschko et al., 2000) can be adopted to eliminate the tensile instability completely, while for rank deficiency, an effective hourglass suppression algorithm by Ganzenmüller (2015) can be implemented relatively easily. Additionally, another variation of structural modeling using SPH is Hamiltonian SPH (HSPH), which provides the flexibility of modeling different elastic and hyperelastic materials by replacing the strain energy function in the momentum equation (Gotoh et al., 2021). For simulating FSI problems, several researchers have attempted to use SPH in both fluid and solid modeling. For example, Antoci and co-workers (Antoci et al., 2007) have modelled both fluid and solid media using SPH and compared the SPH results against their experimental data. Moreover, the TLSPH method for solid modeling has been implemented in some recent FSI models (Sun et al., 2021; O'Connor and Rogers, 2021) to avoid the tensile instability in the solid body. HSPH has also been extended into solving FSI problems (Khayyer et al., 2018). In fact, other numerical techniques can be coupled with SPH to solve FSI problems as well. For example, SPH has been coupled with FEM (Yang et al., 2012; Fourey et al., 2017; Hermange et al., 2019), as the latter is commonly regarded as the highly specialized solver for solid modelling.

Most of the solvers mentioned above for solid modeling are continuum-based which require the use of complex constitutive equations. In fact, a typical solid mechanics problem can also be simulated using discrete methods such as Lattice Spring Models (LSMs) that do not require the conventional solid constitutive equations. This kind of

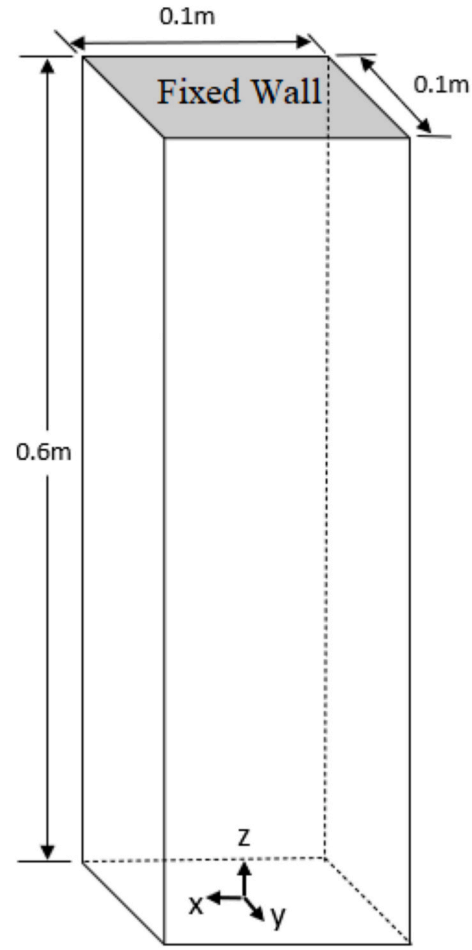

Fig. 3. Geometry of the hanging beam.

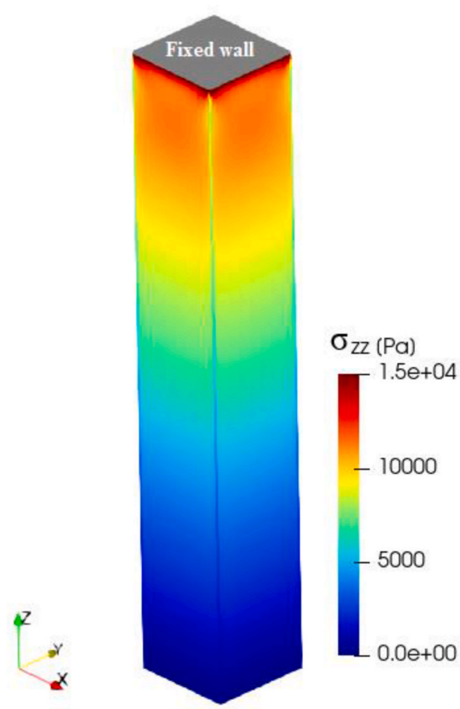

Fig. 4. Normal stress developed within the hanging beam due to self-weight at t = 5 s. Dp = 0.0025 m.

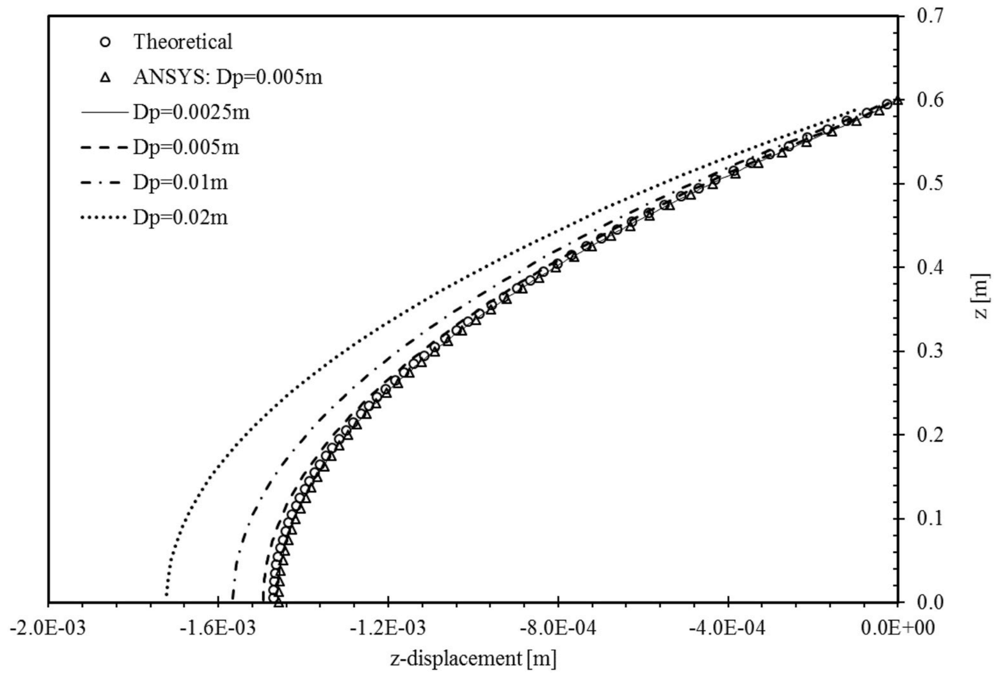

(a)

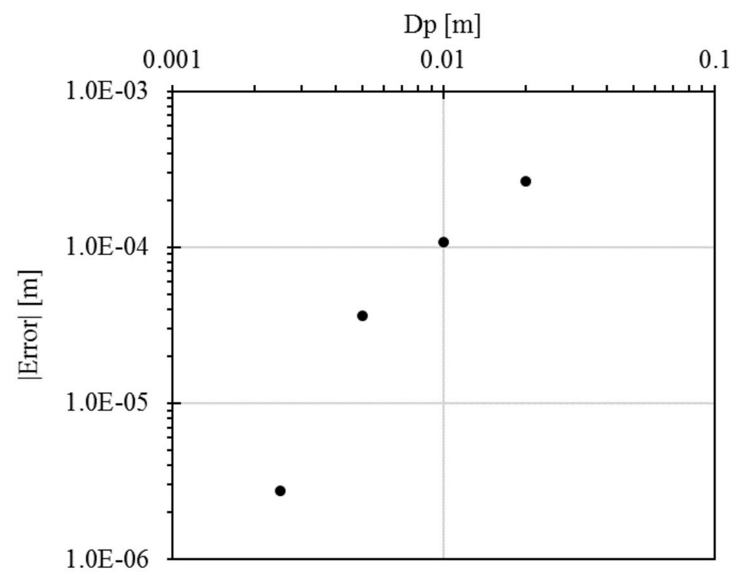

(b)

Fig. 5. (a) The displacement along the axial (z-) direction of the hanging beam using different particle sizes (Dp). (b) Spatial convergence error plot where the error is measured against the grid-independent FEM solution at the free end (x = y = z = 0 m).

discrete methods, in fact, are very suitable for simulating problems involving solid fracture by selectively removing the spring bond between particles. One of the popular LSM models is the Discrete Element Method (DEM), which has been widely used to model collisions between two approaching bodies. Lately, some researchers have extended DEM to model deformation within a flexible solid body and coupled DEM with SPH to model FSI problems (Tang et al., 2018; Wu et al., 2016; Nasar et al., 2019). Most of the discontinuous methods, however, are applicable only for a narrow range of Poisson ratio to ensure non-negative spring stiffness values. In this respect, another LSM method known as Volume Compensated Particle Method (VCPM) (or known as Lattice Particle Method (LPM)) (Chen et al., 2014) has been developed to handle a wider range of Poisson ratios. Very recently, VCPM has been coupled with SPH to simulate a series of 2D FSI problems (Ng et al., 2020, 2022). Its energy conservation property has been extensively studied and the SPH-VCPM method has been coupled with DEM as well to model fluid-solid mixture flow problems (Ng et al., 2021).

Most of the aforementioned SPH-based FSI schemes are implemented in two-dimensional (2D) space; however, a 2D model might not accurately capture the actual flow physics in a complex domain. For example, the 2D SPH-DEM model proposed by Tang and co-workers (Tang et al., 2018) could not capture the secondary currents in

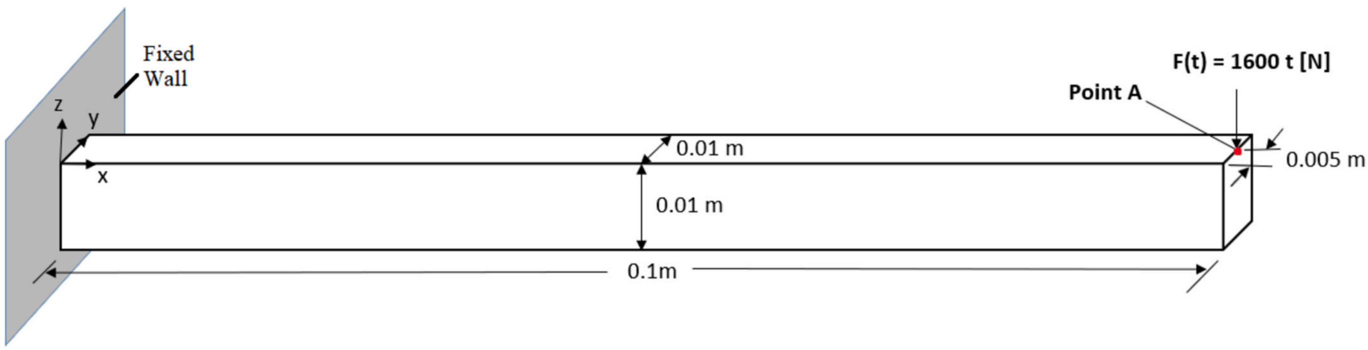

Fig. 6. Geometry of the beam subjected to a dynamic loading F(t) at Point A.

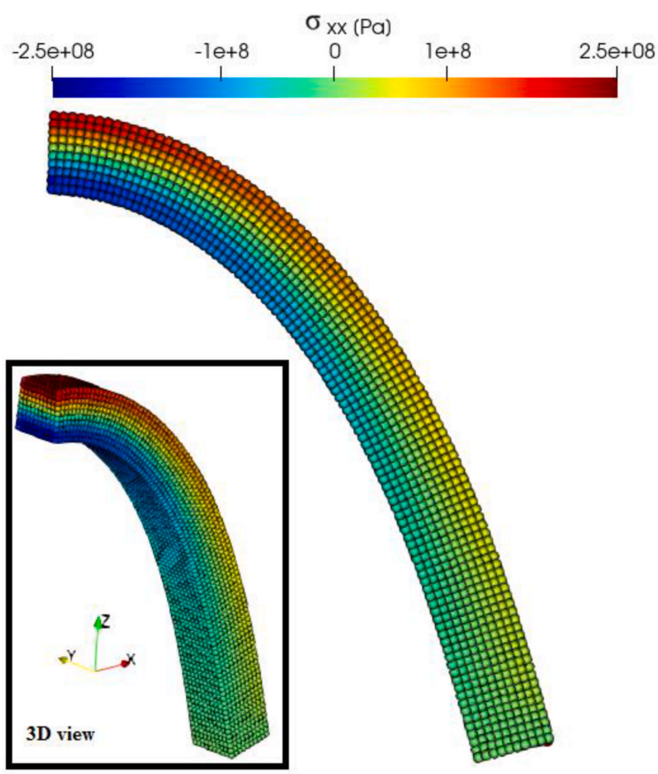

Fig. 7. Normal stress in the deformed cantilever beam at t = 0.48 s due to dynamic loading. Dp = 0.001 m.

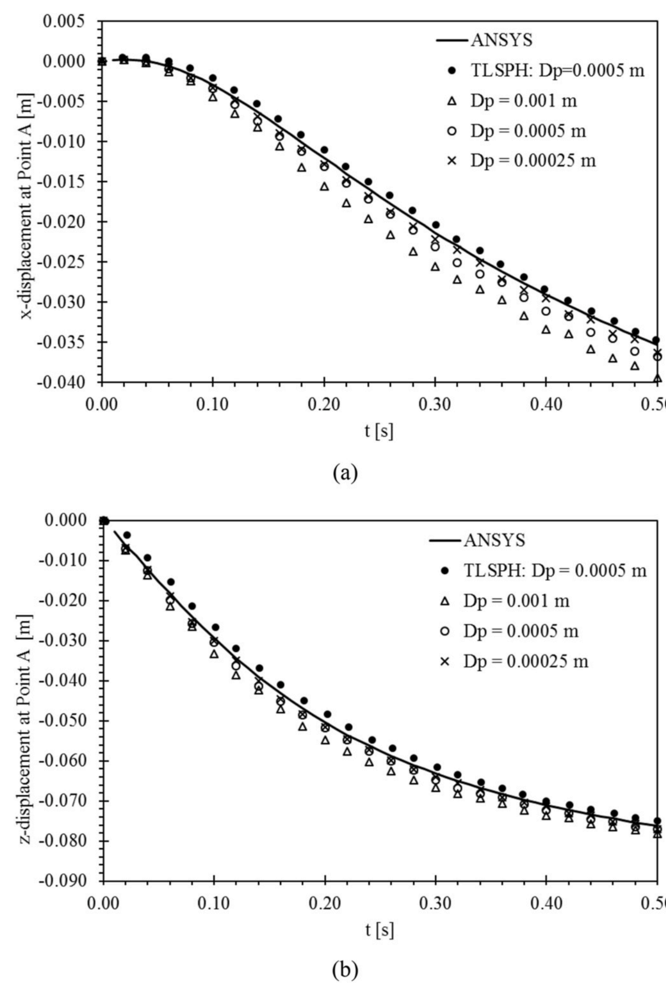

Fig. 8. Time histories of deflection for the cantilever beam at point A: (a) x-displacement and (b) z-displacement.

scouring. To date, several authors have coupled SPH with either mesh-based or particle-based method for simulating three-dimensional (3D) FSI problem. Hermange and co-workers (Hermange et al., 2019) have coupled FEM with SPH to study complex phenomena of tire hydroplaning in 3D. Zhan and co-workers (Zhan et al., 2019) have developed the GPU-accelerated WCSPH-TLSPH scheme for simulating 3D FSI problems and compared the computational efficiencies between WCSPH and TLSPH. They found that the particle simulation time per step (referred to as GPU_{factor} in their work) of TLSPH is one order of magnitude higher than that of WCSPH. Very recently, TLSPH has been implemented in the open-source SPH code DualSPHysics (Crespo et al., 2015) for simulating 2D and 3D FSI problems (O'Connor and Rogers, 2021). Sun and co-workers (Sun et al., 2021) have introduced different time resolutions in solid and fluid bodies and integrated the solid and fluid equations sequentially in order to enhance the computational efficiency of their 3D FSI solver. They have also pointed out the importance of considering the 3D effects in certain FSI benchmark cases. From the current trend, due to the massive computational cost requirement of particle methods, the 3D extension of a SPH-based FSI solver is often accompanied with parallel computing through GPU (O'Connor and Rogers, 2021; Zhan et al., 2019), which could be owing to the superiority of GPU (vs. multiple CPUs) in terms of energy consumption and pricing. A more comprehensive review on Lagrangian meshfree framework for both solid and fluid solvers for FSI can be found in the recent work by Gotoh and co-workers (Gotoh et al., 2021).

In this work, the 2D SPH-VCPM method previously developed and presented in (Ng et al., 2020, 2022) is extended to three dimensions with the overarching goal to study more challenging FSI problems that involve material failure. As the first step, we present the work on

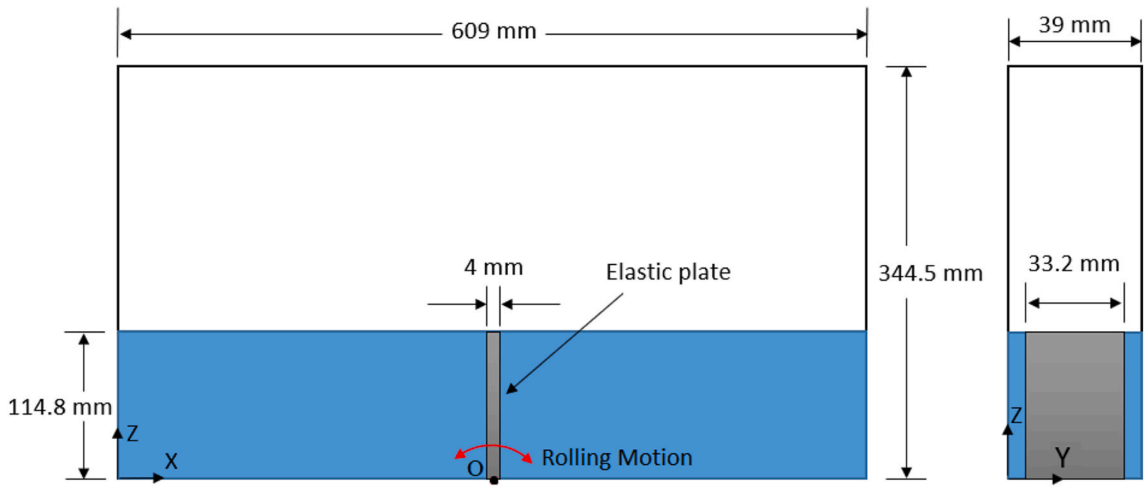

Fig. 9. Geometric details (front and side views) of an elastic plate attached to the bottom of a rolling tank partially filled with oil.

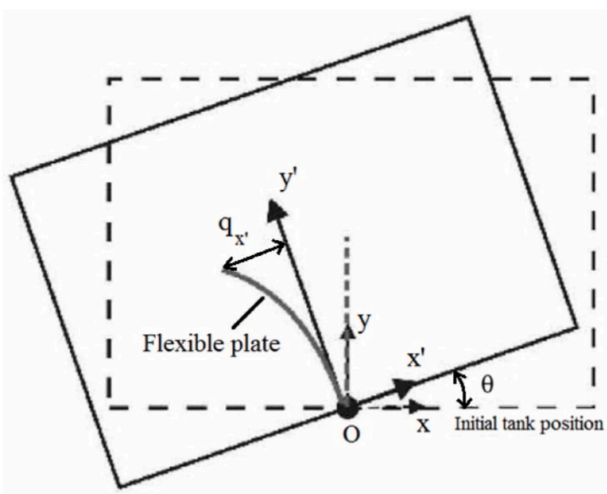

Fig. 10. The definition of local x'-displacement ($q_{x'}$) as the flexible plate is deformed in the rolling tank. Picture is taken from (Ng et al., 2020).

verifying and validating the proposed 3D FSI modeling methodology in this paper. In order to model these 3D FSI problems at realistic scales, the VCPM method is implemented in the open-source SPH code DualSPHysics in the current work, whose performance has been optimized for both CPU and GPU (Crespo et al., 2015). Recently, O'Connor and Rogers (O'Connor and Rogers, 2021) have implemented the Total Lagrangian SPH approach in DualSPHysics as well to simulate 3D FSI problems. Compared to their work, the major improvement from this research is the implementation of multiple time-stepping scheme in DualSPHysics so that the computational efficiency of the FSI solver is enhanced. Apart from performing validations using classical benchmark cases, the 3D numerical results from this research are also compared against those of new benchmark cases recently put forward by Yilmaz and co-workers (Yilmaz et al., 2021, 2022) in which the 2D numerical result and experimental data have been made available. It is believed that our 3D FSI model generated for replicating the recent experimental observation of Yilmaz and co-workers (Yilmaz et al., 2022) is the first-ever reported 3D computational model at the time of writing, and it is found that this 3D model is able to capture the free surface patterns more accurately as compared to the 2D model. The computational performance of VCPM is also reported and discussed. Finally, preliminary results regarding the capability of SPH-VCPM method in handling FSI problem involving solid rupture is demonstrated.

2. Governing equations and numerical method

2.1. Flow model

The weakly-compressible SPH (WCSPH) approach implemented in

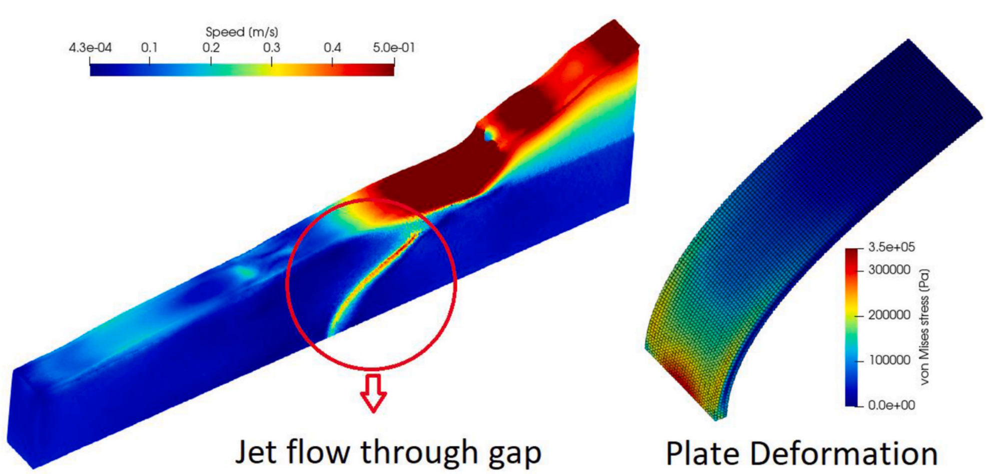

Fig. 11. Snapshot of the velocity field at t = 2.5 s for the three-dimensional sloshing flow (left) and close-up of the plate deformation (right) in the rolling tank study.

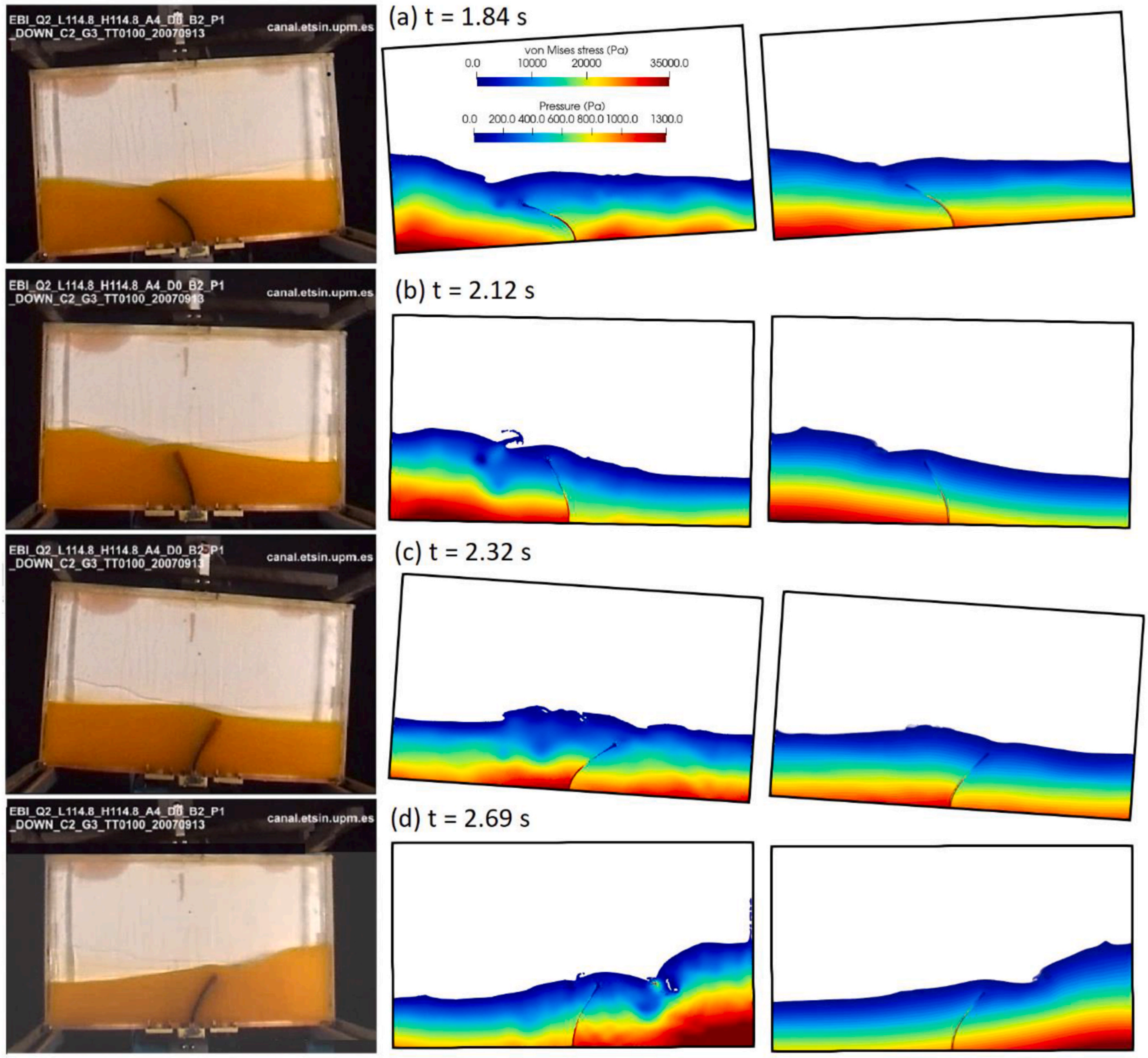

Fig. 12. Qualitative comparison of snapshots taken at various stages of the sloshing flow obtained from experiment (Souto-Iglesias et al., 2008; Paik and Carrica, 2014) (left column), 2D SPH-VCPM method (center column) and 3D SPH-VCPM method (right column).

DualSPHysics is used to model the fluid dynamics. The mass balance equation of fluid flow can be written as:

$$\frac{d\rho}{dt} = -\rho \nabla \cdot \mathbf{v}, \tag{1}$$

where ρ is the fluid density and $\mathbf{v}$ is the fluid velocity vector. By using the SPH approximation, the mass balance equation of a fluid particle i can be discretized as:

$$\frac{d\rho_i}{dt} = \rho_i \sum_j V_j (\mathbf{v}_i - \mathbf{v}_j) \cdot \nabla_i W_{ij} + 2\delta h c^F D_i \ . \tag{2}$$

Here, V_j is the volume of neighbouring particle j, $\nabla_i W_{ij} = \frac{dW_{ij}}{dr} \frac{\mathbf{r}_{ij}}{\mathbf{r}_{ij}}$ and $\mathbf{r}_{ij} = \mathbf{r}_i - \mathbf{r}_j$. For all the cases considered here, the Wendland kernel function W_{ij} (Wendland, 1995) with a compact support radius $r_c = 2h$ is employed. The smoothing length h is set as $1.5 \times Dp$, where Dp is the initial particle spacing. When using WCSPH, the pressure of a fluid particle i is explicitly computed using an equation of state (Monaghan, 1994):

$$P_i = \frac{\rho^F (c^F)^2}{\gamma} \left(\left(\frac{\rho_i}{\rho^F} \right)^{\gamma} - 1 \right) , \tag{3}$$

with the polytrophic index γ set as 7 and ρ^F indicating the initial fluid density. It is important to ensure that the fluid speed of sound c^F to be at least $10\mathbf{v}_{\max}$ so that the fluid density fluctuations can be kept to approximately 1% of the reference density, thus leading to a quasi-incompressible flow behavior. Here, $\mathbf{v}_{\max}$ is the anticipated maximum flow speed.

The density diffusion term $2\delta h c^F D_i$ is introduced in the R.H.S. of Equation (2) to suppress the pressure noise typical of WCSPH schemes, and δ is usually taken as 0.1 (Antuono et al., 2012). The term D_i is computed by using the density diffusion approach recently proposed by

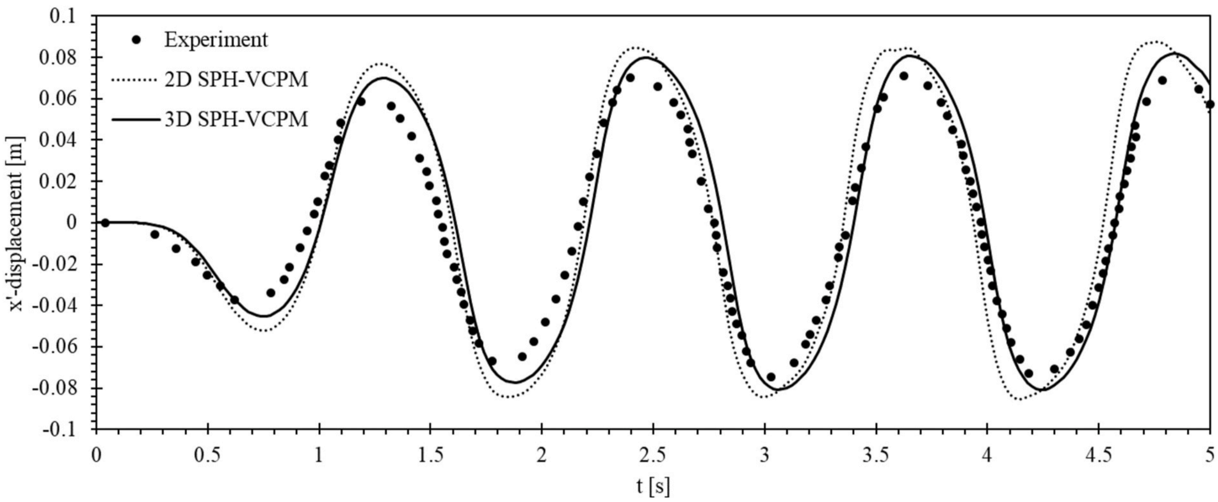

Fig. 13. x'-displacement of the tip of the elastic plate clamped to the bottom of a rolling tank. Experimental data is obtained from (Souto-Iglesias et al., 2008).

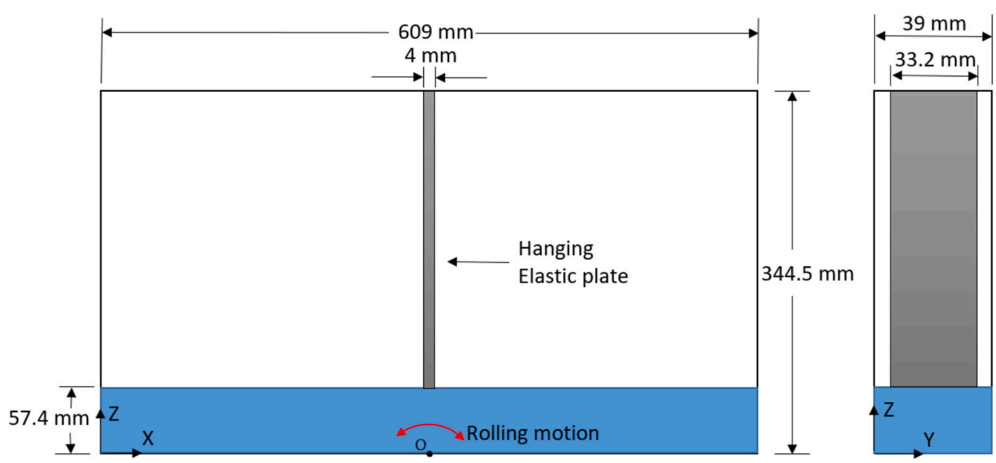

Fig. 14. Geometric details (front and side views) of a hanging elastic plate in a tank partially filled with water and subjected to rolling motion.

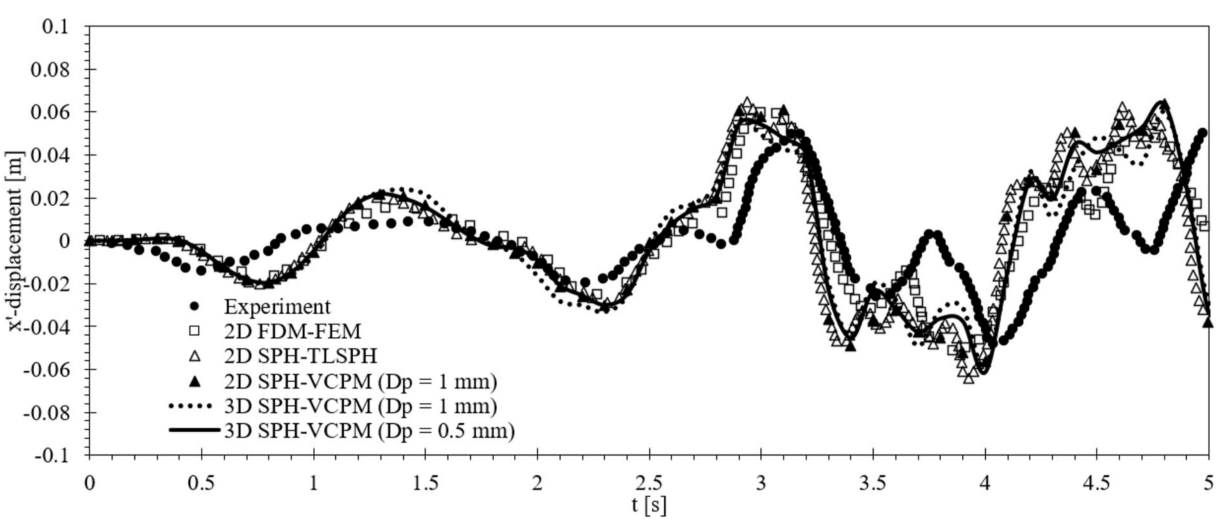

Fig. 15. x'-displacement of the tip of the hanging plate predicted using various numerical methods: 2D FDM-FEM (Paik and Carrica, 2014), 2D SPH-TLSPH (O'Connor and Rogers, 2021) and the current SPH-VCPM method. Experimental data is obtained from (Idelsohn et al., 2008).

Fourtakas and co-workers (Fourtakas et al., 2019), which is known for its capability to restore the consistency near the free surface without having to compute the renormalized gradient (Antuono et al., 2012).

The momentum balance equation of fluid particle i can be expressed as:

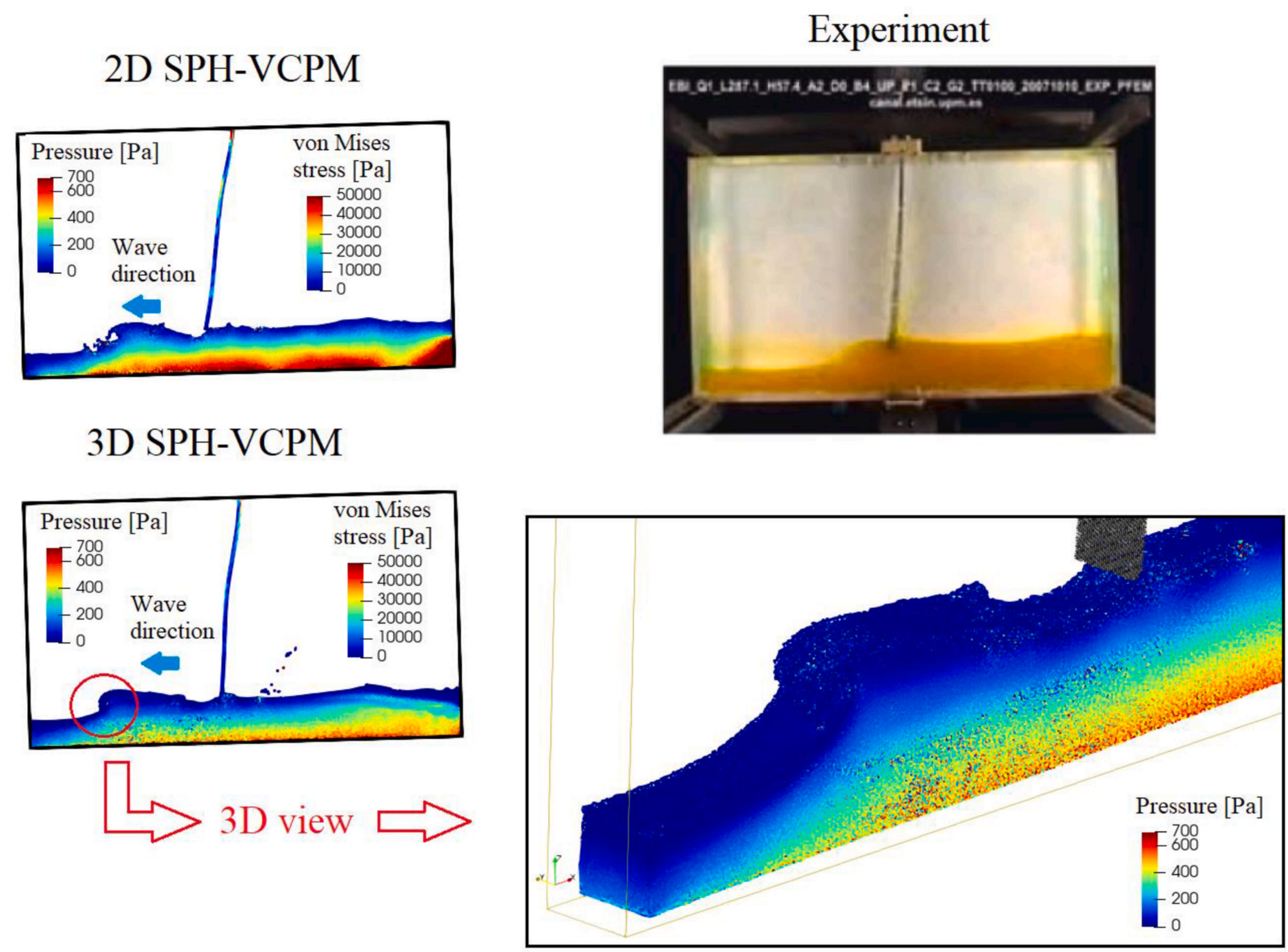

Fig. 16. Snapshot of particles' pressure at t = 3.8 s predicted using 2D and 3D SPH-VCPM methods and visual comparison against the experimental data (Idelsohn et al., 2008).

$$m_i \frac{d\mathbf{v}_i}{dt} = \mathbf{F}_i \ , \tag{4}$$

where $\mathbf{F}_i$ is the net force vector acting on a fluid particle i. Both the pressure force $\mathbf{F}_{P,i}$ and viscous force $\mathbf{F}_{V,i}$ are primary forces in fluid dynamics. Other external force such as weight $\mathbf{F}_{ext,i} = m_i\,\mathbf{g}$ can be included, where $\mathbf{g}$ is the gravitational acceleration vector. Therefore, the net force vector can be written as:

$$\mathbf{F}_i = \mathbf{F}_{P,i} + \mathbf{F}_{V,i} + \mathbf{F}_{ext,i} \ . \tag{5}$$

Note that in the current work, the fluid particle mass m_i is treated as constant. Using SPH approximations, the pressure and viscous forces can be written respectively as:

$$\mathbf{F}_{P,i} = -\sum_j V_i V_j (P_i + P_j) \nabla_i W_{ij} \tag{6}$$

and

$$\mathbf{F}_{V,i} = \sum_j m_i m_j \frac{4\nu^F}{\rho_i + \rho_j} \frac{\nabla_i W_{ij} \cdot \mathbf{r}_{ij}}{\left(\mathbf{r}_{ij}^2 + 0.01h^2\right)} \mathbf{v}_{ij} + \sum_j m_i m_j \left(\frac{\overline{\overline{\tau}}_i}{\rho_i^2} + \frac{\overline{\overline{\tau}}_j}{\rho_j^2} \right) \nabla_i W_{ij} \ . \tag{7}$$

The first and second summation terms appearing in the R.H.S. of Equation (7) represent the laminar and turbulent viscous forces, respectively, where the turbulent stress tensor $\overline{\overline{\tau}}$ is modelled using the Large Eddy Simulation (LES) approach in (Dalrymple and Rogers, 2006). For the modelling of laminar viscous force, the fluid kinematic viscosity ν^F is prescribed.

On the wall boundary condition, the dynamic boundary condition (DBC) (Crespo et al., 2007) is adopted as it is well-known for its robustness in simulating complex free-surface problem. For density update, the wall particles follow the same mass balance equation of fluid particles. The pressure values of wall particles can then be computed using the state equation.

2.2. Solid model

The 3D Volume Compensated Particle Method (VCPM) (or known as Lattice Particle Method (LPM)) (Chen and Liu, 2016) is implemented in DualSPHysics to model the deformation of linear elastic solid. Unlike SPH, VCPM is more beneficial in modelling solid body since the motion of a solid particle is purely dependent on its first and second nearest neighbours, i.e., the same set of neighbours throughout the course of a simulation if solid fracture is not modelled. Furthermore, VCPM uses 1D bond-level force-elongation relationship, which avoids the use of complex constitutive equation as needed in continuum-based approaches such as FEM.

In the current work, the 3D Simple Cubic (SC) lattice structure (Chen and Liu, 2016) is implemented in DualSPHysics as the SC configuration is compatible with the Cartesian particle layout generated by GenCase, the pre-processor of DualSPHysics. As depicted in Fig. 1, for a generic

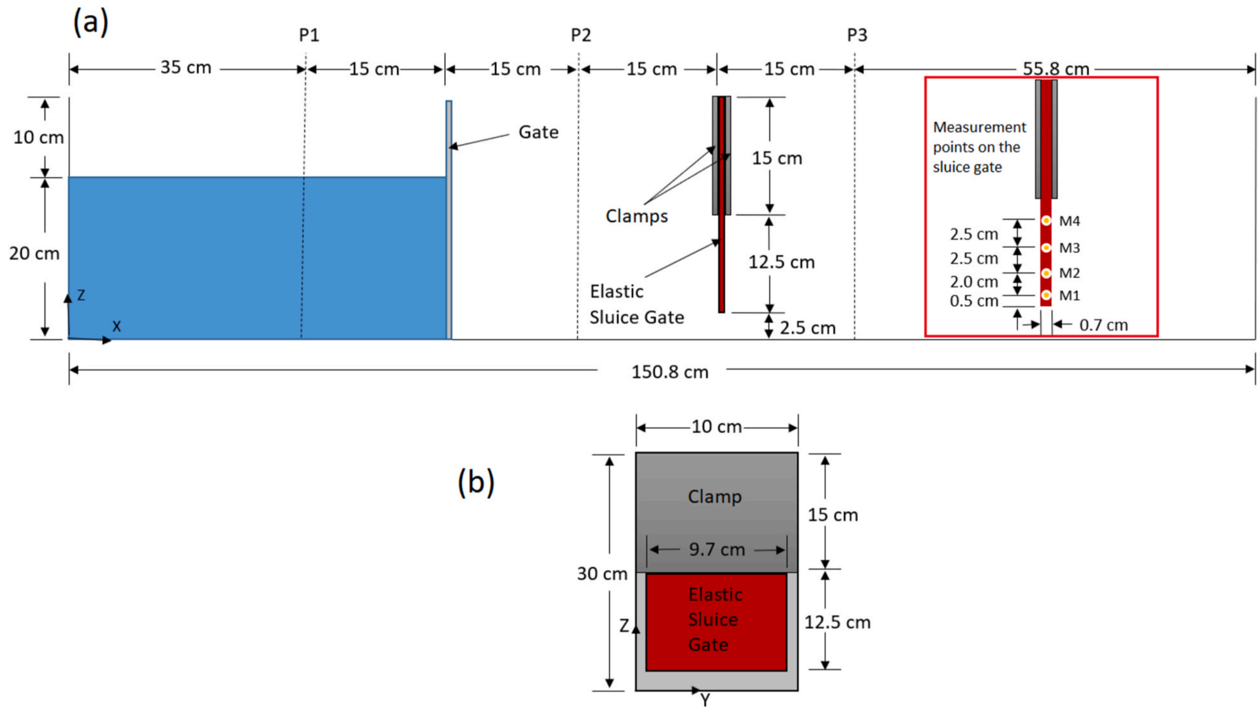

Fig. 17. Geometric details of the elastic sluice gate subjected to dam break flow: (a) front view; (b) side view of the elastic sluice gate assembly.

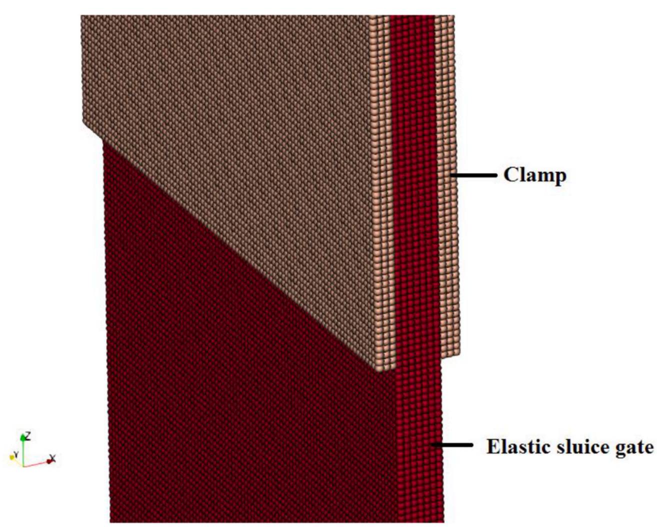

Fig. 18. Details of the particles' layout in the clamp and sluice gate domains.

flexible solid particle I, there are 6 first and 12 s neighbours at distances Dp and $\sqrt{2}\ Dp$ away from particle I, respectively. For modelling the elastic behaviour of a solid body, bonds are created between the particle I and all its neighbours. By ensuring energy equivalency between the VCPM description and its continuum counterpart, the values of bond stiffness can be expressed in terms of material elastic properties (Chen and Liu, 2016):

$$k = \frac{2RE}{1+\upsilon^S}\ , \tag{8}$$

where E is Young's modulus, υ^S is Poisson ratio and $R = 0.5\ Dp$. In order to remove the restriction of Poisson ratio, a non-local parameter T is introduced and can be determined in terms of material elastic properties as (Chen and Liu, 2016):

$$T = \frac{RE(4\upsilon^S - 1)}{\left(9+4\sqrt{2}\right)(1+\upsilon^S)(1-2\upsilon^S)}\ . \tag{9}$$

Upon identifying the positions of all particles using GenCase, a separate algorithm is developed in order to establish the bonds connecting all particles within the flexible solid body. Whenever necessary, bonds are created between the flexible solid and the neighbouring fixed and moving boundary particles in order to model the clamping of the respective flexible solid body. This bond network is generated only once, and it is then stored in memory and used to compute the forces between VCPM particles by using the procedure outlined in the following paragraphs.

The equations of motion for a solid particle I can be written as:

$$m_I \frac{d\mathbf{v}_I}{dt} = \mathbf{F}_{S,I} + \mathbf{F}_{F\to S,I} + \mathbf{F}_{ext,I}\ , \tag{10}$$

where $\mathbf{F}_{S,I}$ is the net spring force, $\mathbf{F}_{F\to S,I}$ is the hydrodynamic force mapped onto the solid particle I and $\mathbf{F}_{ext,I}$ is the sum of external forces (e.g., gravity). For a steady-state problem, a damping force term, which is dependent on the Young's modulus E (Zhan et al., 2019), can be included in $\mathbf{F}_{ext,I}$ as well:

$$\mathbf{F}_{ext,I} = m_I \mathbf{g} - m_I \sqrt{\frac{E}{\rho^S (Dp)^2}}\mathbf{v}_I\ , \tag{11}$$

where the first and second terms on the R.H.S. of Equation (11) are the weight and the damping force, respectively. Here, the mass of the solid particle is fixed as $m_I = \rho^S (Dp)^D$, where Dp is the initial solid particle spacing (same as the initial fluid particle spacing in the current work). Moreover, ρ^S is the density of the solid body and D is the number of dimensionalities of the problem.

The net bond force $\mathbf{F}_{S,I}$ can be determined based on the total energy of a particle in VCPM as (Chen and Liu, 2016):

$$\mathbf{F}_{S,I} = \sum_J f_{IJ} \widehat{\mathbf{u}}_{IJ}\ , \tag{12}$$

where $\widehat{\mathbf{u}}_{IJ} = (\mathbf{r}_I - \mathbf{r}_J)/\mathbf{r}_I - \mathbf{r}_J$ is the unit bond vector and f_{IJ} is the bond

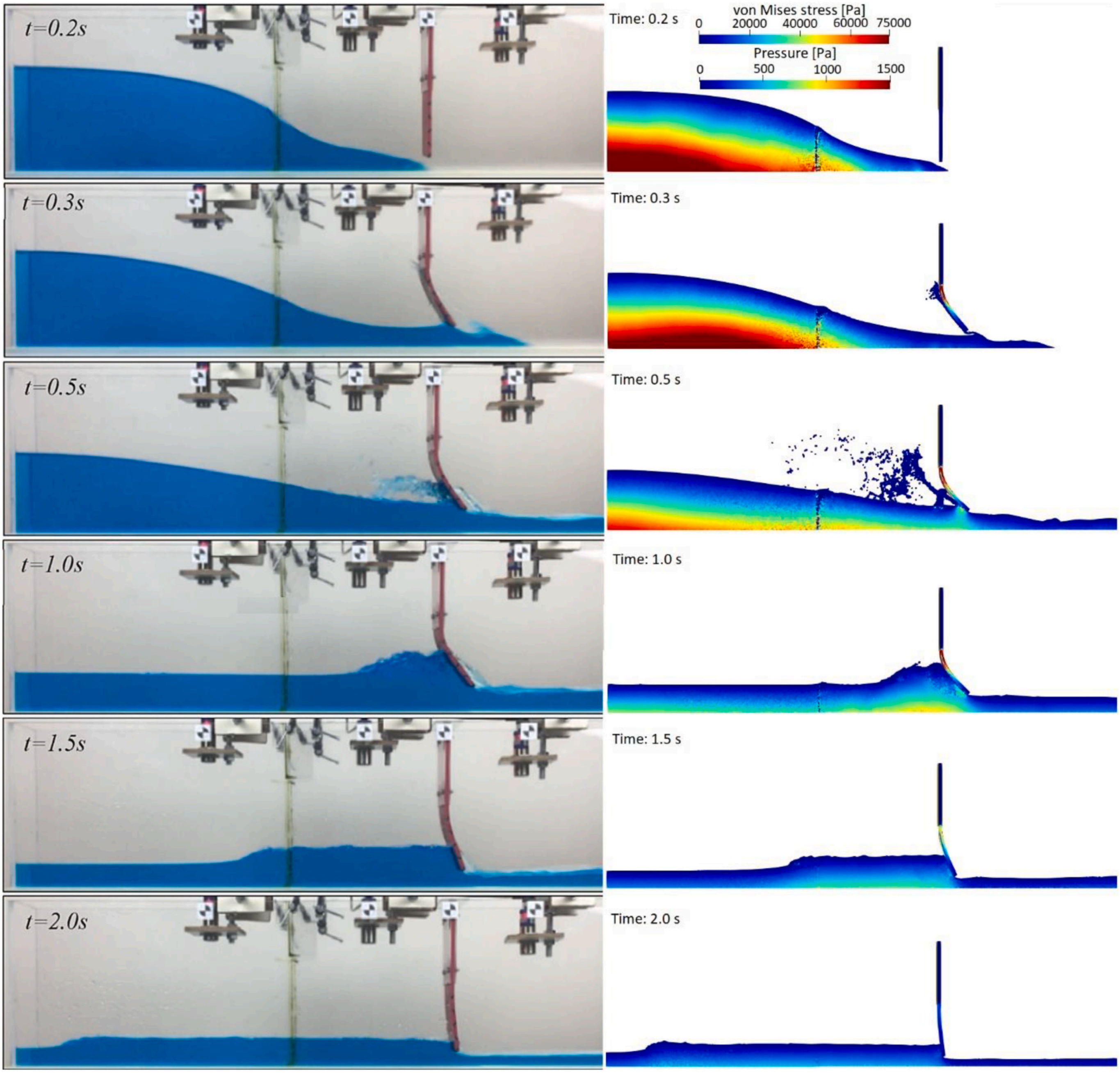

Fig. 19. Comparison of flow sequences: experimental photos from (Yilmaz et al., 2021) (left) and results predicted using the current 3D SPH-VCPM method (right).

force that has the following explicit form:

$$f_{IJ} = -k\delta l_{IJ} - \frac{T}{2}\left(\sum_{Q}\delta l_{IQ} + \sum_{M}\delta l_{JM}\right), \tag{13}$$

where δl_{IJ} is half of the elongation of the bond between solid particles I and J. Note that Equation (13) involves not only the local particles I and J, but also their respective neighbours Q and M. More details about VCPM can be found in our earlier works (Chen et al., 2014; Ng et al., 2020).

In the following subsections, the hydrodynamic force acting on the solid particle I, i.e., $\mathbf{F}_{F\to S,I}$ will be discussed.

2.3. Fluid-structure coupling

To enforce the non-penetration and no-slip wall boundary conditions at the fluid-solid interface, the solid particles near the fluid-solid interface act as dummy particles in the DualSPHysics SPH solver. Here, the pressure of dummy/solid particle I, P_I, near the fluid-solid interface is calculated based on the Dynamic Boundary Condition (DBC) approach (Crespo et al., 2007). Following this, the pressure and viscous forces acting on a fluid particle i due to the neighbouring dummy/solid particle I can be determined respectively as:

$$\mathbf{F}_{P,I\to i} = -V_i V_I (P_i + P_I)\nabla_i W_{iI} \tag{14}$$

and

$$\mathbf{F}_{V,I\to i} = m_i m_I \frac{4\nu^F}{\rho_i + \rho_I}\frac{\nabla_i W_{iI}\cdot\mathbf{r}_{iI}}{\left(\mathbf{r}_{iI}^2 + 0.01h^2\right)}\mathbf{v}_{iI} + m_i m_I\left(\frac{\overline{\overline{\tau}}_i}{\rho_i^2} + \frac{\overline{\overline{\tau}}_I}{\rho_I^2}\right)\nabla_i W_{iI} \tag{15}$$

Note that ρ_I is calculated based on the DBC approach by solving the mass balance equation. The volume of a dummy particle I, V_I, can then

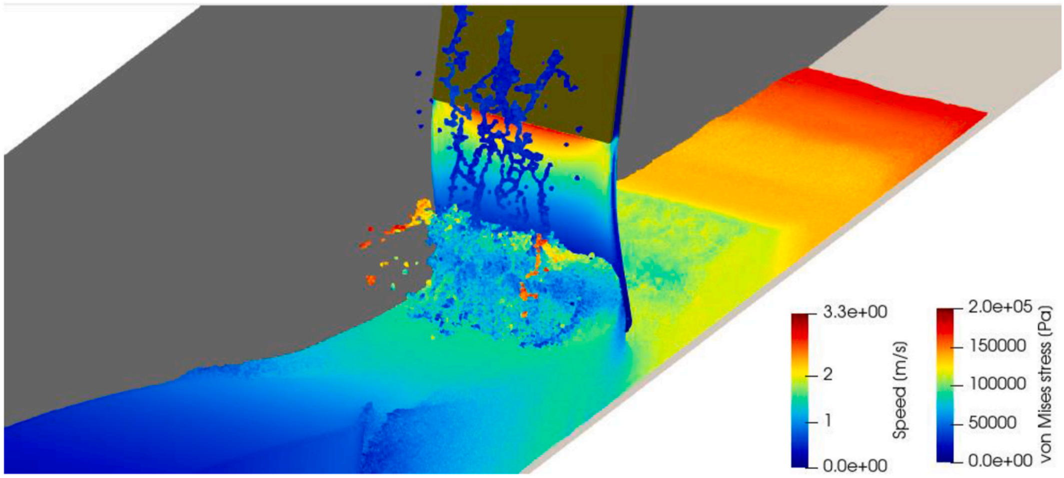

Fig. 20. Splashing of fluid particles behind the sluice gate at t = 0.38 s. The gate reopens upon the second wave impact.

be computed accordingly as $V_I = \frac{m_i}{\rho_I}$, where m_i is the mass of an interacting fluid particle. Since the solid particle I acts as a dummy particle of a fluid particle i, the value of m_I in Equation (15) is computed as $m_I = m_i$. As a result, the total hydrodynamic force exerted on a solid particle I, $\mathbf{F}_{F\rightarrow S,I}$, is expressed as follows:

$$\mathbf{F}_{F\rightarrow S,I} = -\sum_{i\in N_f}\left(\mathbf{F}_{P,I\rightarrow i} + \mathbf{F}_{V,I\rightarrow i}\right) \tag{16}$$

where N_f is the number of fluid particles residing in the circle/sphere of influence of $r_c = 2h$ centered at the solid particle I. The negative sign is introduced before the summation term in the R.H.S. of Equation (16) so that Newton's third law is satisfied.

2.4. *Multiple time-stepping*

2.4.1. *Use of multiple time step size*

In some of the recent WCSPH FSI explicit solvers (O'Connor and Rogers, 2021; Zhan et al., 2019), the time step size Δt is restricted for stability purposes following the relation:

$$\Delta t = \min\left(\Delta t^F, \Delta t^S\right), \tag{17}$$

where Δt^F and Δt^S are the maximum allowable time step sizes for the fluid and solid solvers, respectively. In DualSPHysics, Δt^F is calculated in the following manner:

$$\Delta t^F = 0.1\min\left\{\sqrt{\frac{h}{\mathbf{a}_{imax}}}, \frac{h}{c^F + \left|\frac{h\mathbf{v}_{ij}\cdot\mathbf{r}_{ij}}{r_{ij}^2+0.01h^2}\right|_{\max}}\right\}, \tag{18}$$

where $\mathbf{a}_{imax}$ is the maximum acceleration of fluid particles. If solid dynamics is considered, Δt^S can be determined as:

$$\Delta t^S = 0.8\frac{Dp}{c^S}, \tag{19}$$

where $c^S = \sqrt{\left(B+\frac{4G}{3}\right)/\rho^S}$ is the sound speed in the solid body, with $B = E/3(1-2\nu^S)$ being the bulk modulus and $G = E/2(1+\nu^S)$ being the shear modulus. Although the use of a single time step size for both fluid and solid domains is simple in terms of implementation, its computational efficiency is often questionable as c^S is likely to be larger than c^F in most engineering problems. As a result, a very small global time step size must be adopted for ensuring overall numerical stability while integrating the fluid and solid governing equations explicitly. The other challenge is on how to couple the fluid and solid governing equations while ensuring computational efficiency and stability. Fourey and co-workers (Fourey et al., 2017) have investigated both Parallel Staggered (PS) and Sequential Staggered (SS) coupling schemes. In PS, both fluid and solid solvers progress at the same time upon exchanging information at the fluid-solid interface. In SS, however, the fluid and solid solver progresses sequentially. The fluid solver progresses first upon receiving the solid particle information (e.g., velocity and position). The fluid pressure and viscous forces acting on the solid body (loading) are then calculated, and this information is sent to the solid solver for updating the velocity and position of all solid particles. It has been reported in literature that SS is numerically more stable than PS (Sun et al., 2021; Fourey et al., 2017).

In the current work, we pursue the idea of SS coupling scheme. To enhance the computational efficiency of SS coupling scheme, a multiple time-stepping scheme is implemented in DualSPHysics to enhance the computational efficiency. The schematic diagram is shown in Fig. 2. Upon solving the SPH fluid equations for each time step based on the existing position and velocity information of the flexible solid body, we perform the integer operation: $\omega = \mathrm{int}\left(\frac{\Delta t^F}{\Delta t^S}\right) + 1$ and re-compute Δt^S accordingly using $\Delta t^S = \Delta t^F/\omega$. The hydrodynamic forces acting on all flexible solid particles near the fluid-solid interface are then computed using Equation (16). These mapped hydrodynamic forces that act as the boundary conditions for the VCPM solver are fixed while integrating the solid equations of motion. By using Δt^S, the equations of motion of solid bodies are integrated ω times to achieve time synchronization with the fluid body. In what follows, the details of the numerical implementation of VCPM in DualSPHysics are explained.

2.4.2. *Symplectic scheme for VCPM in DualSPHysics*

Due to the use of multiple time steps as explained in the previous subsection, it is imperative to match the velocity marching interval while integrating the fluid and solid governing equations. Recently, Zhang and co-workers (Zhang et al., 2021) have recommended the use of a position-based Verlet scheme to achieve strict momentum conservation (c.f. Fig. 1 in (Zhang et al., 2021)) as the scheme requires only a single update of velocity within one time step. In fact, this scheme has been implemented in DualSPHysics, and it is more commonly known as the symplectic time integration scheme (Leimkuhler et al., 1996). To ensure the consistency of the time integration schemes implemented in both the fluid and solid domains, the same symplectic scheme implemented in DualSPHysics is used for integrating the equations of motion for a solid body.

Assuming that the fluid governing equations have been integrated using the symplectic time integration scheme in DualSPHysics (i.e. $\mathbf{v}_i^{n+1}$, $\mathbf{r}_i^{n+1}$ and ρ_i^{n+1} have been obtained for all fluid particles) and the hydrodynamic force acting on each solid particle I has been computed

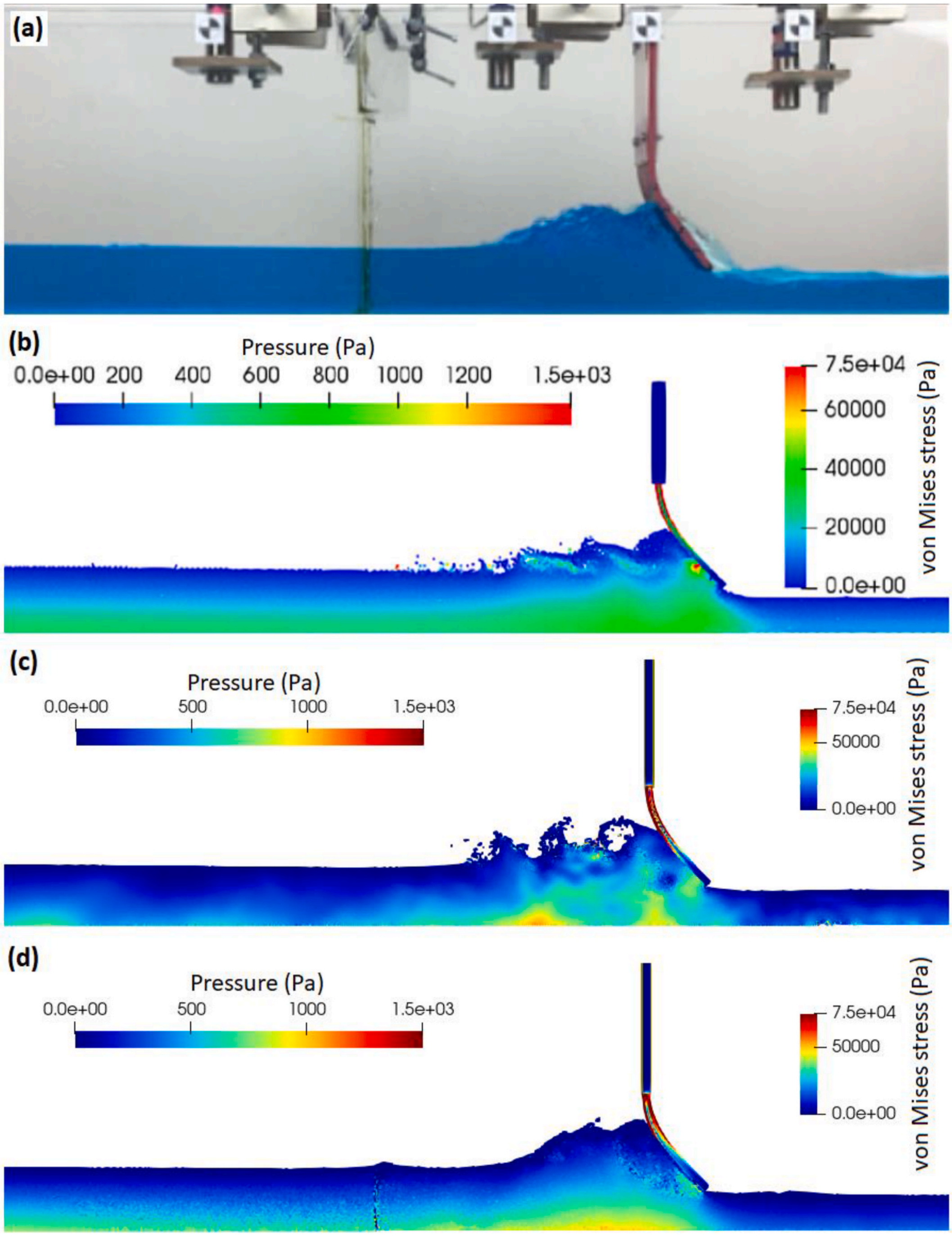

Fig. 21. Free surface patterns behind the sluice gate at t = 1.0 s using various methods: (a) Experiment in (Yilmaz et al., 2021); (b) 2D SPH-FEM (Yilmaz et al., 2021); (c) 2D SPH-VCPM and (d) 3D SPH-VCPM.

using Equation (16), the following steps are carried out in order to solve the solid equations of motion. Note that the mapped hydrodynamic forces on all solid particles *I* near the fluid-solid interface are fixed while integrating the solid equations of motion.

Step 1: By using Equation (10), the acceleration $\left(\frac{d\mathbf{v}_I}{dt}\right)^m$ of a solid particle *I* is computed. Then, its position and displacement at intermediate time step $t^{m+0.5}$ are updated as:

$$\mathbf{v}_I^{m+0.5} = \mathbf{v}_I^m + \frac{\Delta t^S}{2}\left(\frac{d\mathbf{v}_I}{dt}\right)^m \tag{20}$$

$$\mathbf{r}_I^{m+0.5} = \mathbf{r}_I^m + \frac{\Delta t^S}{2}\mathbf{v}_I^m \tag{21}$$

This step is commonly known as the predictor stage in literature.

Step 2: Based on the intermediate position and displacement values obtained from Step 1, the acceleration of the solid particle *I*, i.e. $\left(\frac{d\mathbf{v}_I}{dt}\right)^{m+0.5}$ is calculated again using Equation (10). Next, the position and displacement of the solid particle *I* at t^{m+1} are corrected as:

$$\mathbf{v}_I^{m+1} = \mathbf{v}_I^m + \Delta t^S\left(\frac{d\mathbf{v}_I}{dt}\right)^{m+0.5} \tag{22}$$

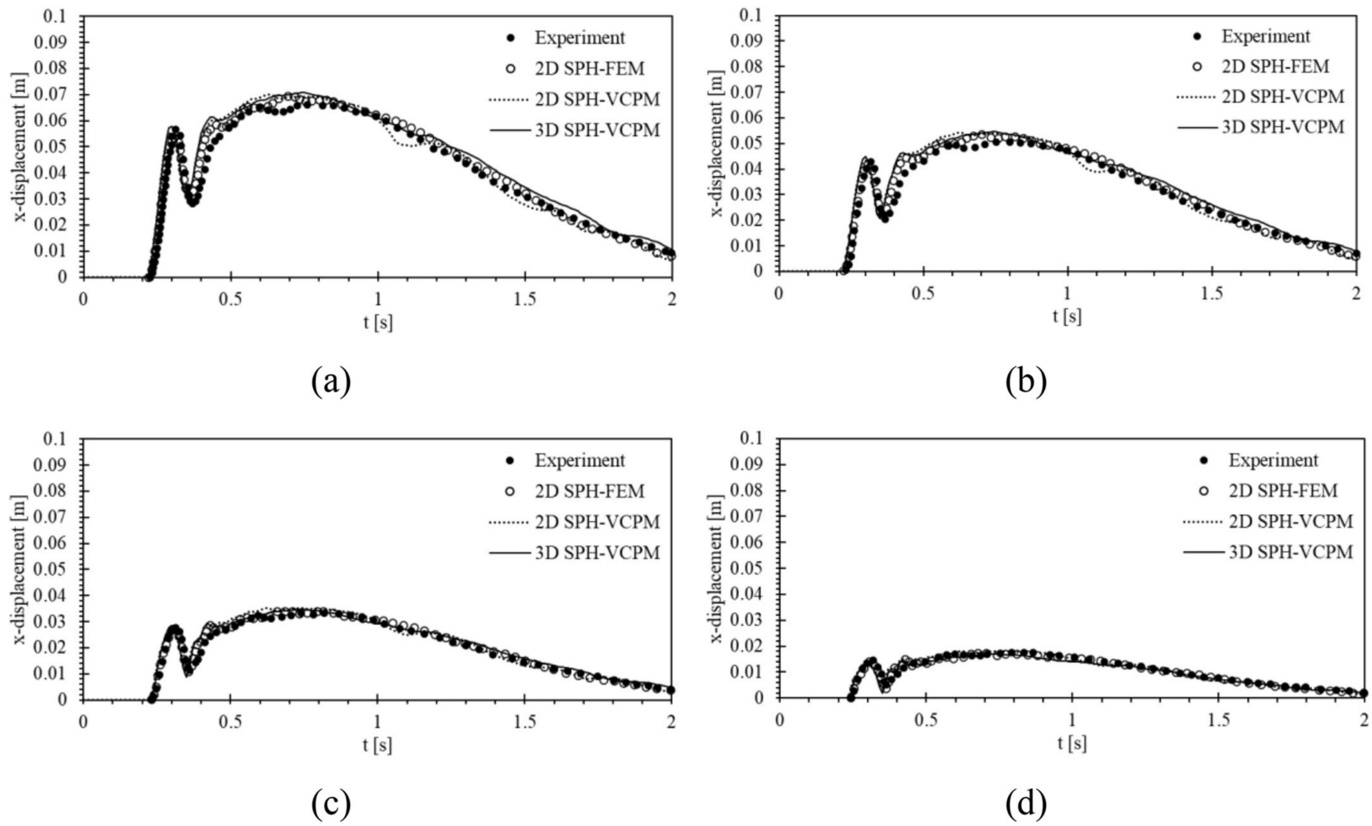

Fig. 22. Deflection in the x-direction at various points of the elastic sluice gate: (a) M1; (b) M2; (c) M3 and (d) M4. Both experimental and 2D SPH-FEM results are obtained from (Yilmaz et al., 2021).

$$\mathbf{r}_I^{m+1} = \mathbf{r}_I^m + \frac{\Delta t^S}{2}\left(\mathbf{v}_I^m + \mathbf{v}_I^{m+1}\right) \tag{23}$$

Step 3: At this point, both ${\mathbf{v}_I}^{m+1}$ and ${\mathbf{r}_I}^{m+1}$ at t^{m+1} may not synchronize perfectly with the fluid flow variables at t^{n+1} if $\omega > 1$. Therefore, Equations (20)–(23) are repeated ω times in order to achieve time synchronization with the fluid body, i.e. $t^{m+\omega} = t^{n+1}$.

Upon synchronizing with the SPH fluid flow solver as outlined in Step 3, the available positions and velocities of all flexible solid particles are fed into the SPH solver in DualSPHysics to initiate the calculation of the next time step.

3. Results and discussions

In this section, several test cases are presented to demonstrate the accuracy of the 3D SPH-VCPM method. Upon validating our implementation of VCPM in DualSPHysics by simulating both static and dynamic solid mechanics problems, the method is then used to simulate several classical FSI test cases as well as the very recent FSI benchmark cases put forward by Yilmaz and co-workers (Yilmaz et al., 2021, 2022). Unless otherwise stated, the gravitational vector **g** is assumed as $<0, 0, -9.81>$ ms^{-2}. All the simulations are performed on an Nvidia Quadro RTX 8000 GPU.

3.1. Beam deformation due to self-weight

Our 3D implementation of VCPM in DualSPHysics is firstly verified by solving a static solid mechanics problem. As shown in Fig. 3, we simulate the deformation of a hanging beam due to its own weight. For this simple problem, the theoretical solution is available.

The simulation is performed until $t = 5$ s so that the quasi steady-state condition can be obtained, accomplished by activating the damping term in Equation (11). The material properties of the beam are: $\rho^S = 2500$ kgm^{-3}, $E = 3$ MPa and $\nu^S = 0.3$. As the beam is supported at the upper end ($z = 0.6$ m) where the displacement is fixed, the local stress level (evaluated using (Chen, 2019)) is relatively high as shown in Fig. 4. The stress decreases along the negative z-direction and drops to almost zero at the lower/free end ($z = 0$ m).

The beam deformations predicted using different particle resolutions are compared against the theoretical solution (Goodier and Timoshenko, 1970) as shown in Fig. 5(a). The 3D VCPM solution approaches the theoretical one as Dp is refined. Nevertheless, our 3D VCPM results obtained using the finest resolution ($Dp = 0.0025$ m) is slightly higher than the theoretical solution and the difference becomes more apparent near the free end. This discrepancy is mainly due to the difference in boundary conditions (imposed at the upper end of the beam) considered in the theoretical model (Goodier and Timoshenko, 1970) and our numerical model. In the current numerical model, the displacements at the upper end are fixed whereas in the theoretical model, the constant-stress condition is applied (Goodier and Timoshenko, 1970). In order to confirm this, we have simulated the same problem by adopting the boundary condition in our numerical model while running the Finite Element Method (FEM) solver in ANSYS. Similar to our current VCPM model, the mesh-independent displacement values simulated using FEM are slightly higher than the theoretical ones, and the FEM results are very close to our VCPM solution obtained using the finest particle resolution, as shown in Fig. 5(a). The spatial convergence of the z-displacement at the free end ($x = y = z = 0$ m) is shown in Fig. 5(b). Here, the error is measured against the mesh-independent FEM solution. For this simple case, the order of convergence is between 1 and 2.

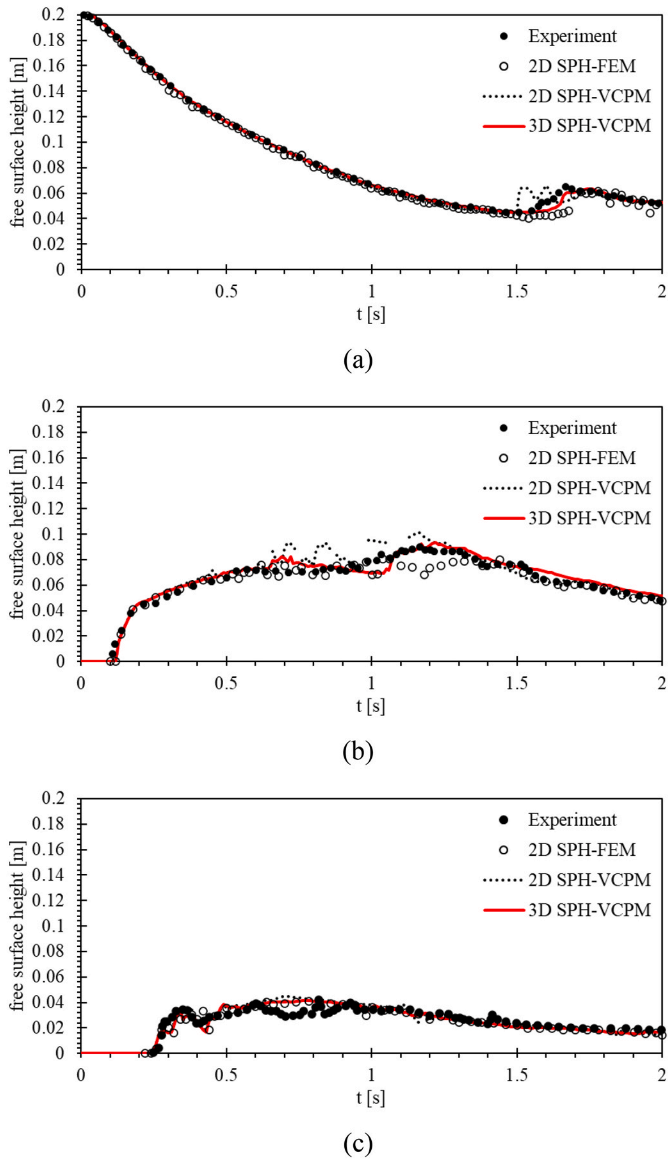

Fig. 23. Free surface elevation at various stations: (a) P1; (b) P2; and (c) P3. Both experimental and 2D SPH-FEM results are obtained from (Yilmaz et al., 2021).

3.2. Beam deformation due to dynamic loading

Next, the 3D VCPM method is applied to simulate a dynamical solid mechanics problem involving very large deformations. Fig. 6 shows the configuration details of the cantilever beam where the displacements are fixed at one end and a concentrated dynamic force $F(t) = 1600t$ [N] (t in second) is acting at the other (free) end of the beam (Point A). Following (Zhan et al., 2019), the material properties used in this example are set as: $\rho^S = 7800$ kgm^{-3}, $E = 2.1$ GPa and $\nu^S = 0.3$. The simulation is executed until $t = 0.5$ s. For this problem, no analytical solution is available and hence we have verified our results against the recently published TLSPH solution of Zhan and co-workers (Zhan et al., 2019) and the FEM solution obtained from the commercial software ANSYS. Zhan and co-workers (Zhan et al., 2019) have compared their TLSPH results against the FEM solution generated using the commercial FEM software package ABAQUS. When comparing both FEM solutions of ANSYS and ABAQUS (Zhan et al., 2019) using $Dp = 0.001$ m, it has been found that results are in very close agreement.

Fig. 7 shows the normal stress level at $t = 0.48$ s and it is found that the stress distribution is quite similar to that of the stabilized TLSPH method (Zhan et al., 2019). Unlike TLSPH, our current VCPM method does not require any additional damping/stabilization term in ensuring the regularity of the solid particles. The time-dependent displacements at Point A are shown in Fig. 8 and the results are compared against the FEM solutions (obtained from ANSYS using $Dp = 0.001$ m). It is interesting to note that the time evolutions of the displacements at Point A during the course of dynamic loading agree considerably well with the FEM and TLSPH (Zhan et al., 2019) solutions. As the particle resolution is refined, our 3D VCPM solution converges well to the FEM solution.

3.3. Oil sloshing in a rolling tank with an elastic plate

This classical FSI test case, which involves an elastic plate clamped at the bottom of a tank undergoing rolling motion, has been physically tested and simulated by Souto-Iglesias and co-workers (Souto-Iglesias et al., 2008). Due to the periodic rolling motion, fluid sloshing occurs within the tank and hence the elastic plate is deformed accordingly. From the experimental data, the plate deformation appears to be quite large and hence it is interesting to test the capability of the current 3D FSI method in simulating this problem.

The material properties of the elastic plate are: $\rho^S = 1100$ kgm^{-3}, $E =$ 6 MPa and $\nu^S = 0.45$. Fig. 9 shows the geometric details of the problem. It can be noticed that the width (measured along the y-direction) of the tank is relatively small as compared to its length and height. This implies that the side walls might affect the overall flow field significantly, promoting flow diffusion/damping effect due to the formation of 3D boundary layers near the side walls. The associated flow damping effect is further exacerbated when the fluid viscosity is high. In the current SPH simulation, an oil of density $\rho^F = 917$ kgm^{-3} and kinematic viscosity $\nu^F = 5 \times 10^{-5}$ m^{2}s^{-1} is employed. For the rolling motion of the tank, the time history of the rolling angle θ (see Fig. 10) is extracted directly from (Souto-Iglesias et al., 2008) in order to correctly model the moving boundary conditions of the tank wall at different time steps. The particle spacing Dp is set to 1 mm, which is adequate to attain a converged solution (Hermange et al., 2019). As such, the total number of particles is approximately 4.2 million for this case.

Fig. 11 shows the jet flow through the small gap between the elastic plate and the side wall. This high-speed oil current which is partially driven by the shearing action between the deforming plate and the rolling side wall would ultimately interact with the free surface and the 3D boundary layer in the vicinity of the side walls. This important flow feature could not be modelled in our previous 2D FSI work (Ng et al., 2020). According to (Bouscasse et al., 2013), the boundary layer formations near the side walls tends to produce additional flow damping effect on the global flow field. This has been witnessed in our current 3D work as well, as reported in Fig. 12. Therein, 2D results are associated with more dynamic oil sloshing and even breaking waves which are visible in Fig. 12 (b) and (d). These flow features captured from 2D simulations are not apparent in the experimental photos. Remarkably, the free surface evolution predicted from the current 3D SPH-VCPM method agrees considerably well with experimental observations.

Fig. 13 shows the time history of the x'-displacement (see the coordinate system in Fig. 10) at the tip of the elastic plate. In general, the displacement amplitude predicted by the 3D model is smaller than that of the 2D model. The lower amplitude could be due to less dynamic oil sloshing in the 3D model. If compared to the 2D results, the 3D results are in better agreement with the experimental data as depicted in Fig. 13. As the flow is highly viscous in the current test case, the accuracy of the 3D results can be further improved by implementing a more accurate wall model in DualSPHysics, e.g. the extrapolation of dummy particle velocity based on wall velocity (Adami et al., 2012) and the modified DBC (English et al., 2021) for all boundary particles, including the floating ones defined in DualSPHysics.

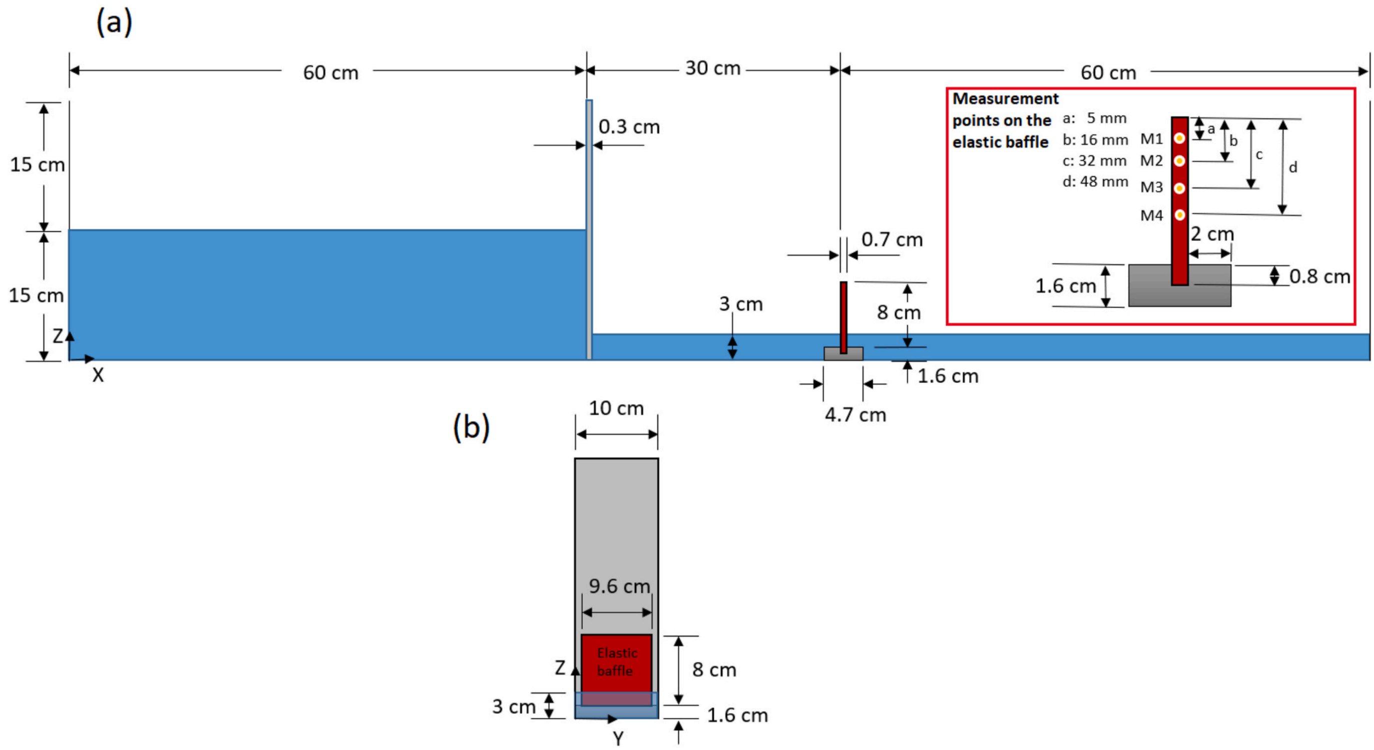

Fig. 24. Geometric details of the elastic baffle in a wet bed. (a) front view; (b) side view of the elastic baffle assembly.

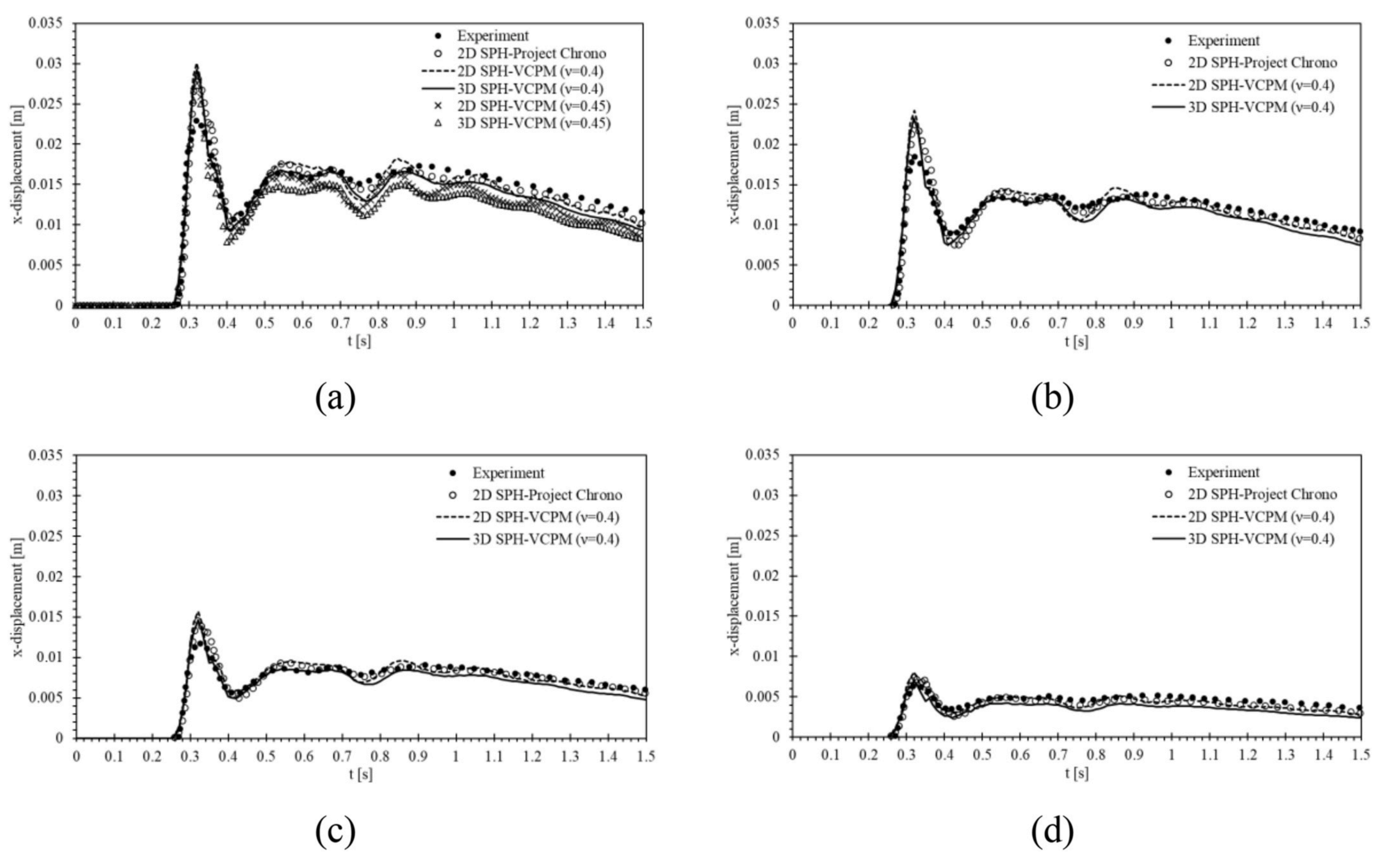

Fig. 25. Deflection in x-direction at various points of the elastic baffle: (a) M1; (b) M2; (c) M3 and (d) M4. Both experimental and SPH-Project Chrono results are obtained from (Yilmaz et al., 2022).

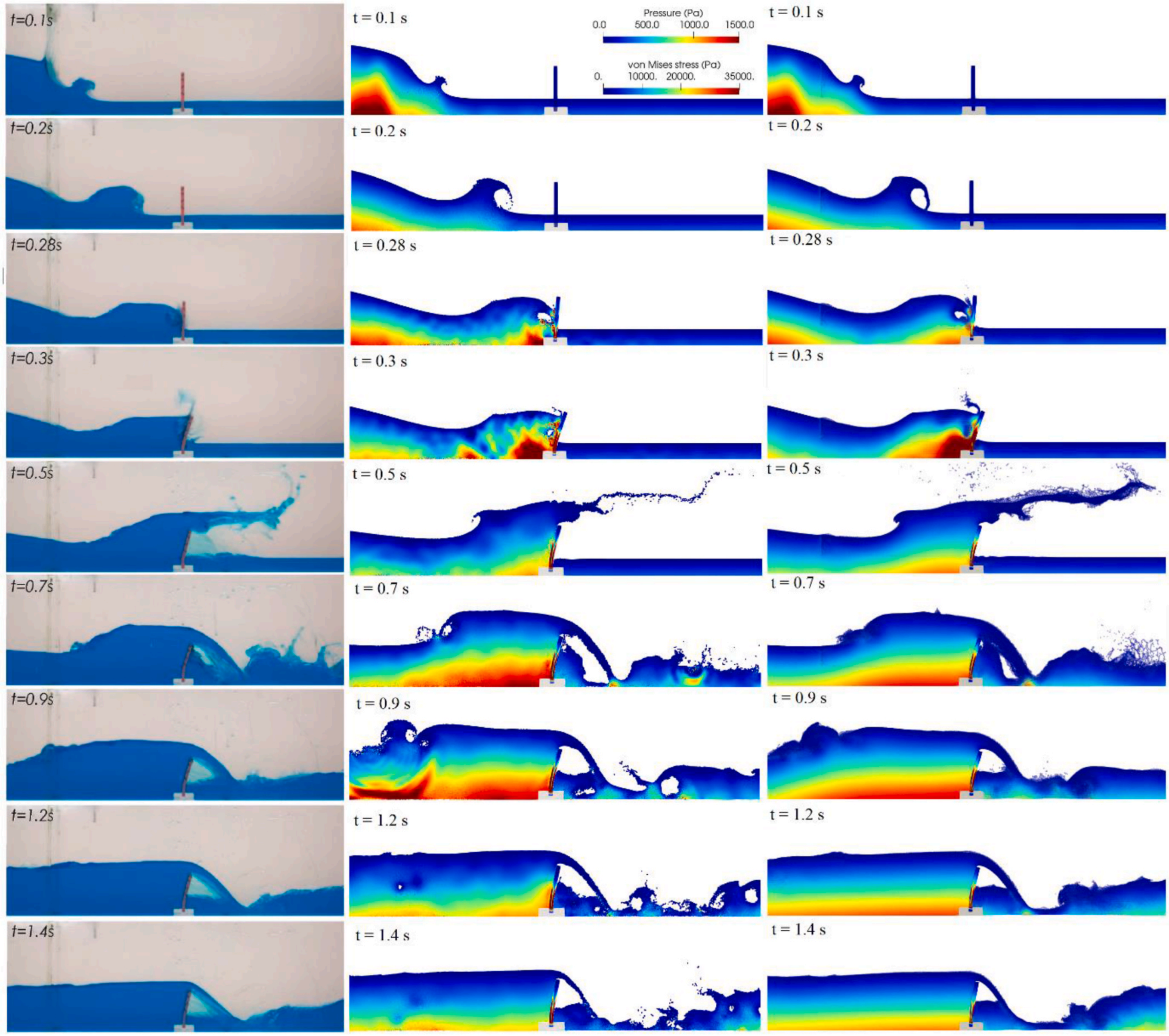

Fig. 26. Comparison of flow sequences: experiments in (Yilmaz et al., 2022) (left); 2D SPH-VCPM method (center); and 3D SPH-VCPM method (right).

3.4. Hanging plate in a rolling tank

This is another classical FSI test case whereby the experimental data is available (Idelsohn et al., 2008). The tank geometry is similar to that of Section 3.3, except that the plate clamped at the bottom is now replaced by a flexible plate of thickness 4 mm and height 287.1 mm which is hung at the top of the tank as shown in Fig. 14. From the experimental data (Idelsohn et al., 2008), the frequency of the plate deformation is quite high at the later stage of sloshing. Unlike the test case in Section 3.3, as the plate is hung at the top of the tank, fluid-structure interaction occurs only when the water wave hits the plate. This has led to a more complex dynamics of the plate.

The material properties of the flexible plate are: $\rho^S = 1900$ kgm^{-3}, $E = 4$ MPa and $\nu^S = 0.45$. Instead of using oil, the working fluid is changed to water, with density $\rho^F = 998$ kgm^{-3} and kinematic viscosity $\nu^F = 1 \times 10^{-6}$ m^{2}s^{-1}. To the best of our knowledge, most of the previous numerical studies on this test case were conducted in 2D (O'Connor and Rogers, 2021; Paik and Carrica, 2014; Idelsohn et al., 2008). In the current work, the study is extended to 3D using our current SPH-VCPM method. To model the rolling motion of the tank, the time history of the rolling angle is extracted from (Idelsohn et al., 2008) in order to mimic the experimental condition and allow a correct benchmarking of the numerical results.

Fig. 15 shows the x'-displacement (see its definition in Fig. 10) at the tip of the hanging beam. It is found that our 2D SPH-VCPM result is almost similar to that obtained using the 2D SPH-TLSPH FSI solver recently implemented in DualSPHysics ($Dp = 0.5$ mm) (O'Connor and Rogers, 2021). Meanwhile, our current 3D SPH-VCPM results are quite close to the 2D results, and within the spread of other previous numerical predictions such as the 2D Finite Difference Method - Finite Element Method (FDM-FEM) (Paik and Carrica, 2014) and the 2D SPH-TLSPH method (O'Connor and Rogers, 2021). As shown in Fig. 15 for the 3D SPH-VCPM results (using $Dp = 0.5$ mm and $Dp = 1.0$ mm), in general, the sensitivity of the particle size on the overall time history of the plate displacement is not very apparent during the initial stage ($0 < t < 1$ s). Nevertheless, as the plate starts to have stronger interaction with the wave arisen from the rolling motion thereafter, some minor discrepancies are spotted on the time gradient of the plate displacement

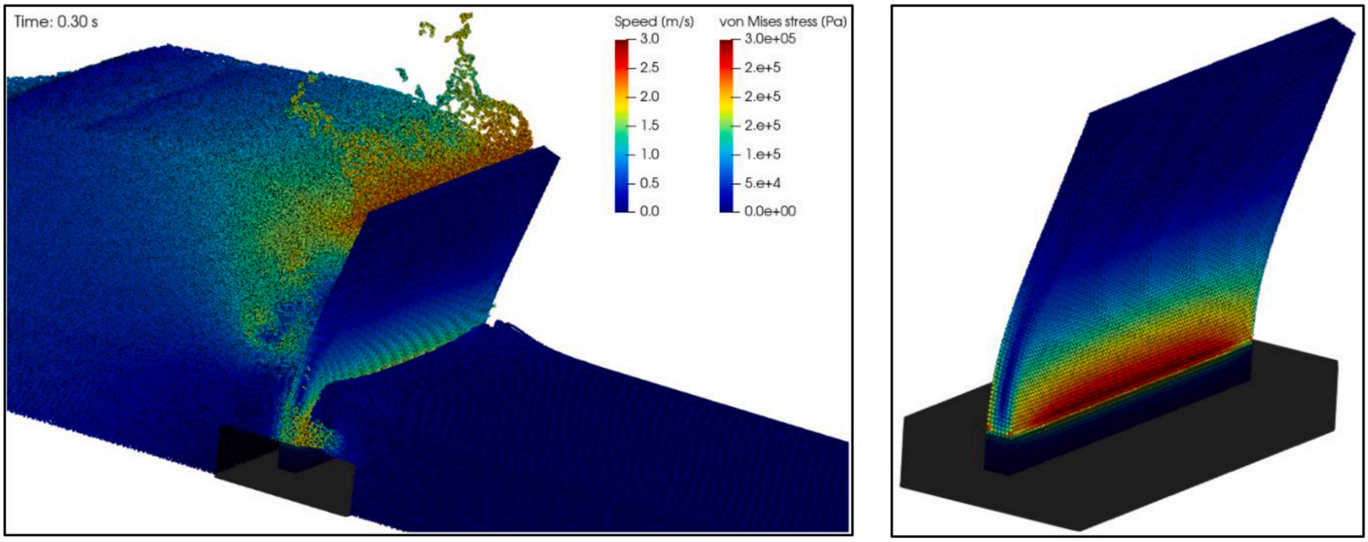

Fig. 27. Three-dimensional views of fluid and solid particles at t = 0.3 s: fluid pressure and von-Mises solid stress representation (left); von-Mises stress within the rubber baffle (right).

Table 1
Simulation time for the 3D beam deformation due to self-weight (Section 3.1).

Resolution [m]	No of particles	Total simulation time [s]	No. of time step	VCPM particle simulation time per step [s]	Simulation time per step [s]
0.02	750	2.9	10048	3.912E-07	0.000293
0.01	6000	6.1	20096	5.042E-08	0.000303
0.005	48000	32.6	40192	1.688E-08	0.000810
0.0025	384000	571.6	80384	1.852E-08	0.007111

Table 2
Simulation time for the 3D beam deformation due to dynamic loading (Section 3.2).

Resolution [m]	No of particles	Total simulation time [s]	No. of time step	VCPM particle simulation time per step [s]	Simulation time per step [s]
0.001	10000	291.8	301010	9.693E-08	0.000969
0.0005	80000	906.9	602019	1.883E-08	0.001506
0.00025	640000	11890.3	1204037	1.543E-08	0.009875

ranging from $t = 1.3$ s to $t = 2.3$ s (i.e., as the plate interacts with the wave and travels from one far end to another) and the small-scale fluctuations in the later stages of sloshing. It is generally expected that the convergence can be improved by refining the particle size as the degree of unphysical boundary layer thickening (due to the use of DBC) near the structure can be further alleviated. Other more accurate wall boundary modelling techniques can be considered as well for improving the convergence ((Adami et al., 2012) (English et al., 2021)).

All numerical predictions agree very well in the early stage of the computation ($0 < t < 1$ s). By judging the crest and trough of the physically measured displacement curve (Idelsohn et al., 2008) at $t > 3$ s, it seems that there is a phase lag between the physical and the simulated results. As shown in Fig. 16, this phase lag could be due to the wave bore (responsible for deforming the hanging plate) which is predicted to be consistently ahead of the physically observed. In fact, this phase lag has also been observed by Khayyer and co-workers in their very recent multi-resolution SPH work (c.f. Figs. 15 and 17 in (Khayyer et al., 2021)), which deserves further attention in the future. From Fig. 16, it seems that the 3D SPH-VCPM model captures the experimentally observed non-breaking wave quite well, while the 2D SPH-VCPM result is accompanied by unphysical wave breaking.

3.5. Wave impact on elastic sluice gate

Recently, Yilmaz and co-workers (Yilmaz et al., 2021) have conducted a physical experiment to investigate the wave impact on an elastic sluice gate. This test case is interesting yet challenging as it involves multiple flow impacts on the sluice gate occurred at different time instants and the generation of hydraulic jump behind the gate as it retraces.

The geometric details of the experiment are depicted in Fig. 17. As noticed, there is a small gap between the sluice gate and the side walls to avoid friction between them. There are three measurement stations (P1–P3) placed at different x-locations to measure the free surface height. Meanwhile, in order to measure the deflection of the sluice gate, four marker points (M1-M4) are placed at different locations of the gate. The locations of measurement stations and marker points are detailed in Fig. 17.

In order to determine the Young's modulus of the rubber-like sluice gate, Yilmaz and co-workers (Yilmaz et al., 2021) have measured the deformation due to the body weight of the sluice gate. These deformation values have then been used to determine the Young's modulus based on the Euler-Bernoulli beam theory. From their findings, the Young's modulus is $E = 4$ MPa. The gate density and Poisson ratio are given as $\rho^S = 1250$ kgm^{-3} and $\nu^S = 0.4$, respectively. Yilmaz and co-workers (Yilmaz et al., 2021) have further simulated this problem using the SPH-FEM approach available in the commercial software LS-DYNA, where SPH and FEM are used for modeling the fluid and solid domains, respectively. Here, they have modelled the problem as 2D and employed the artificial viscosity approach to stabilize the SPH scheme. In their work, the particle resolution has been set to $Dp = 2$ mm. The water density and kinematic viscosity have been set as $\rho^F = 1000$ kgm^{-3} and $\nu^F = 1 \times 10^{-6}$ m^{2}s^{-1}.

In the current work, we extend the numerical study of Yilmaz and co-workers (Yilmaz et al., 2021) to 3D by using the SPH-VCPM approach. Instead of using the originally proposed particle resolution of 2 mm (Yilmaz et al., 2021), we have refined the particle resolution Dp to 1 mm in order to better resolve the thickness of the elastic sluice gate (= 0.7 cm). As such, the total number of particles is ~13.5 million. Fig. 18 shows the particle layouts in both the clamp (modelled as fixed

Table 3
Simulation times for the 3D FSI problems.

Case	No. of particles	Total sim. time [s]	SPH sim. time [s]	VCPM sim. time[a] [s]	VCPM sim. time[b] [s]	SPH particle sim. time per step [ns]	VCPM particle sim. time per step[a] [ns]	VCPM particle sim. time per step[b] [ns]
Sect. 3.3: 3D Oil Sloshing- Beam at the bottom ($Dp = 1$ mm)	4,223,520[c] 15,048[d]	19,587	19117.6	469.4	376.8	16.2	46.1	24.1
Sect. 3.4: 3D Water Sloshing – Hanging Beam ($Dp = 1$ mm)	2,907,597[c] 37,884[d]	18,931	17632.3	1298.9	1218.6	11.8	36.6	32.5
Sect. 3.5: 3D sluice gate ($Dp = 1$ mm)	8,415,709–13,528,104[c] 183,540[d]	34,904	33733.6	1170.3	1051.0	15.3–24.6	25.5	21.5
Sect. 3.6: 3D wet-bed dam break ($Dp = 1$ mm)	15,609,262[c] 59,185[d]	47,753	47368.4	384.4	298.4	18.3	28.0	19.3

[a] $\mathbf{F}_{F\to S,I}$ (Equation (16)) + VCPM (Steps 1–3 in Section 2.4.2).
[b] VCPM (Steps 1–3 in Section 2.4.2).
[c] Number of SPH particles.
[d] Number of VCPM particles.

particles) and the elastic sluice gate sub-domains. At the interface between the clamp and the sluice gate, spring-like bonds are established between the clamp and sluice gate particles in order to model the contact between them. Yilmaz and co-workers (Yilmaz et al., 2021) have employed the artificial viscosity approach in their 2D SPH-FEM model. However, it is known that the artificial viscosity parameter is subjected to tuning based on the nature of the problem and particle resolution. Therefore, in our current 3D FSI model, the Laminar + LES model available in DualSPHysics is used to resolve the flow diffusion.

Fig. 19 compares the free surface patterns obtained from both experimental and numerical observations. Due to the fact that the removal of the rigid plate is not modelled in the current work (as the gate removal velocity is not given in (Yilmaz et al., 2021)), it is apparent that the wave-front propagates faster than that observed experimentally at $t = 0.2$ s. The deformation of elastic sluice gate due to the impact of dam-break flow is witnessed at $t = 0.3$ s. Subsequently, complex wave breaking occurs behind the gate, which is accompanied by rigorous three-dimensional splashing of water particles as shown in Fig. 20. The formation of a hydraulic jump is clearly visible behind the sluice gate at $t = 1.0$ s as the dam-break wave interacts with the water particles behind the gate. As time elapses, the wave starts to reflect upstream and the water level behind the gate descends accordingly. As a result, the impact force acting on the gate eases, and the relaxation on the elastic sluice gate is observed as the gate retraces back to its original position. In general, our 3D SPH-VCPM results compare quite well with those observed experimentally. The free surface patterns behind the sluice gate at $t = 1.0$ s are further compared in Fig. 21. As can be seen, when adopting the 2D simulation approach, the motion of the free surface is more violent, which is accompanied by breaking waves. These breaking waves, however, are not apparent from the experimental photo. When compared to the 2D approach, the free surface captured from our 3D simulation approach is less violent and compares quite well against the experimental observation. This could be due to the additional flow damping effect as the side walls are included in the 3D model.

The time histories of the deflection of the elastic sluice gate (Points M1-M4) are compared in Fig. 22. As can be seen, the gate starts to open when the dam-break wave firstly hits the gate at $t \sim 0.21$ s. The deflection peaks at $t \sim 0.3$ s and retraces until $t \sim 0.35$ s, beyond which the deflection increases again due to the incoming water current. The gate opens gradually thereafter and reaches its maximum deflection level at $t \sim 0.75$ s. The gate opening decreases steadily afterwards, as the water level behind the gate eases off when the wave is reflected upstream. From Fig. 22, in general, all the 2D and 3D simulation results are quite close to each other and compare well against the experimental data. Our 2D SPH-VCPM results are slightly noisier than the 3D ones, which could be due to more violent wave-breaking phenomenon observed in the 2D model. Interestingly, this noise is not apparent in the 2D SPH-FEM model that employs the artificial viscosity approach.

The free surface heights at stations P1–P3 predicted using both 2D and 3D models are compared in Fig. 23. The wiggling time evolution of the free surface is clearly visible in our 2D SPH-VCPM model, particularly at station P2, where it is residing within the hydraulic jump regime. Interestingly, our current 3D SPH-VCPM results are quite smooth and follow closely with the measured free surface heights. At station P1, the delay in the rise of water level after $t = 1.5$ s is quite apparent in the 2D SPH-FEM model. In this regard, by using the 3D SPH-VCPM model, the predicted time instant during which the water level rises abruptly due to the reflecting wave agrees quite well with the experimental data, albeit a slight delay is still observed. At station P2, the wave crest that is observed experimentally at $t \sim 1.2$ s is well resolved using the current 3D SPH-VCPM model. The water heights at station P3 (downstream of the gate) predicted using different models are quite similar to each other and close to the measured data. There is a slight decrease in water height at $t \sim 0.4$ s, which is mainly due to the relaxation of the elastic sluice gate.

3.6. *Wave impact on rubber baffle (wet bed)*

In contrast with the test case presented in Section 3.5, the rubber baffle is now located in a wet bed which is then subjected to wave impact due to dam break. This test case has been recently investigated by Yilmaz and co-workers (Yilmaz et al., 2022) both experimentally and numerically. Due to the rich and complex dynamics involved, it has been recently recommended by Yilmaz and co-workers (Yilmaz et al., 2022) as a suitable benchmark test case for hydroelastic analysis.

Fig. 24 shows the geometrical details of the experimental setup, where a vertical gate is used to separate two water bodies of different initial heights in order to produce the wet bed condition. A rubber baffle, which is mounted to a rectangular block as shown in Fig. 24, is placed 0.3 m downstream from the vertical gate. There is a small gap of 2.0 mm between the baffle and the side wall. Four marker points (M1-M4) are placed at various locations of the baffle (see Fig. 24) to measure the respective x-displacements. Again, Yilmaz and co-workers (Yilmaz et al., 2022) have adopted the Euler-Bernoulli beam theory to estimate the Young's modulus of the rubber baffle, i.e. $E = 5.7$ MPa. The density of the baffle is taken as $\rho^S = 1250$ kgm^{-3}.

In our current numerical model, the initial particle spacing Dp is set as 1.0 mm. The fluid density and kinematic viscosity are prescribed as $\rho^F = 1000$ kgm^{-3} and $\nu^F = 1 \times 10^{-6}$ m^{2}s^{-1}, respectively. For fluid modeling, Yilmaz and co-workers (Yilmaz et al., 2022) have adopted the 2D SPH modelling approach in DualSPHysics, resorting to the artificial viscosity to model flow diffusion. For the elastic baffle modelling, however, they have segmented the baffle into 5 rigid bodies interconnected with a hinge. The rigid body motion of each segmented baffle is then solved using the Chrono library available in DualSPHysics. In the current work, we intend to extend the model to 3D by using our current SPH-VCPM approach. To the best of our knowledge, this is the first ever 3D computational FSI model that replicates this flow case.

In contrast with the previous work of Yilmaz and co-workers (Yilmaz et al., 2022) for the sluice gate problem presented in Section 3.5, the value of the Poisson ratio was not provided for the current model. Therefore, the same value of Poisson ratio reported in their previous work of sluice gate (Yilmaz et al., 2021), i.e., $\nu^S = 0.4$ is adopted in the current model. We have performed a sensitivity analysis of the value of Poisson ratio on the 2D SPH-VCPM model and the results are shown in Fig. 25(a). Indeed, for M1-M4 (see Fig. 25(a–d)), the 2D SPH-VCPM results with $\nu^S = 0.4$ have shown good agreement with the 2D SPH results of Yilmaz and co-workers (Yilmaz et al., 2022). Therefore, we have decided to carry out our 3D simulation using $\nu^S = 0.4$. As shown in Fig. 25, the 3D results under-predict the actual baffle deformation. This could be due to the wall damping effect in the 3D model (due to side walls) as the baffle is partially/fully immersed in the water body during flow impact. In fact, it should be noted that the current linear elastic model may not be able to correctly capture the deformation behavior of rubber-like material. Further study is needed, for example, by implementing more complex material models to study the deformation behavior of the current rubber baffle.

Upon the sudden removal of the vertical gate, the dam-break wave starts to drag the tail water downstream of the vertical gate and a bore is formed. The bore moves downstream towards the elastic baffle and hits the baffle at $t \sim 0.28$ s. This is accompanied by a sudden deflection on various parts of the baffle as shown in Fig. 26. Some degree of relaxation on the baffle can then be seen thereafter, while some water particles overtop the baffle and travel downstream. As such, the water level in the downstream region starts to build up, thus imposing fluid pressure on the leeside of the baffle. This causes the deflection of the baffle to ease off as time elapses, as the water levels on both sides of the baffle start to even out.

As depicted in Fig. 26, the 2D SPH-VCPM results are associated with more dynamic wave breaking at $t > 0.9$ s, particularly in the downstream region. These wave breakings are not apparent in the experimental photo and the 3D model. In fact, we notice that the free surface patterns predicted using our current 3D FSI model tally quite well with the experimental observation at various time frames. Nevertheless, the leakage flow through the small gap between the baffle and the side wall, which is observed experimentally beyond $t = 0.5$ s, is not well resolved in the current 3D model. This could be attributed to the insufficient number of SPH particles used to resolve the small gap (only 2 particles are used). The other reason could be due to the excessive repulsive force caused by the dynamic boundary condition (DBC) in wall modelling that could potentially limit the number of particles that are able to pass through this small gap.

Fig. 27 shows the instantaneous deformation of the baffle when the dam-break wave starts to hit the baffle at $t = 0.3$s. Apart from the overtopping water particles, upstream water particles leak through the small gap (between the side wall and the baffle) at a relatively high speed and interact with the tail water downstream. It is appealing to note that the predicted stress field inside the rubber baffle is smooth.

4. Computational time

The computational times required to execute all the test cases mentioned earlier are listed in Table 1-Table 3. For the pure solid modelling tests using the 3D VCPM method (Table 1-Table 2), in general, it is observed that the VCPM particle simulation time per step (i.e., the total VCPM simulation time per VCPM particle is divided by the total number of VCPM time steps) decreases as the number of particles increases. However, for the static solid modelling test (deformation due to self-weight), the VCPM particle simulation time per step starts to level off and increases slightly when a reasonably fine particle resolution is used. We believe that the scalability of VCPM method could be further improved by managing the shared and global memories in GPU in a more effective manner.

Table 3 shows the simulation times required to execute the 3D FSI cases presented in the current work. Note that the computational times required for input data loading and output data saving are not considered. As shown, the total simulation time of SPH is considerably longer than that of VCPM due to the substantially larger number of SPH particles. Recently, Zhan and co-workers (Zhan et al., 2019) reported that the TLSPH particle simulation time per step (or known as $\mathrm{GPU}_{\mathrm{factor}}$ in their work) is one order of magnitude larger than that of SPH. As compared to TLSPH (Zhan et al., 2019), it is interesting to note that the VCPM particle simulation time per step is in the same order of magnitude as that of SPH implemented in the highly-optimized DualSPHysics solver for all the FSI test cases shown, even when the computation time spent for mapping the hydrodynamic force on VCPM particles near the fluid-solid interface is taken into account (see superscript [a] in Table 3). As compared to TLSPH, we infer that less computational time is needed for a lattice-spring model (e.g., VCPM) as operations such as deformation gradient and stress tensor computations are not required for each time step.

5. Conclusion

In this work, we have extended our previous Fluid Structure Interaction (FSI) solver to 3D by implementing the Volume Compensated Particle Method (VCPM) in the highly optimized open-source SPH code (DualSPHysics) for simulating 3D FSI problems. The main intention of employing VCPM as the solid solver is to allow us to simulate FSI problems involving solid fracture without experiencing singularity-related issue as encountered in continuum-mechanics-based method such as FEM. The Simple Cubic (SC) version of VCPM method has been adopted to model the linear elastic behavior of solid body as the SC lattice structure is fully compatible with the initial SPH particle layout generated using GenCase, the pre-processor of DualSPHysics. For each fluid time step, the SPH fluid equations are solved first, followed by integrating the solid governing equations based on the VCPM algorithm. To enhance the computational efficiency, the solid governing equations are integrated multiple times within a fluid step so that the time levels of both solid and fluid bodies are synchronized.

Compared to our previous works where only simple 2D FSI problems are considered, the current work has witnessed the capability of the new solver in simulating complex 3D FSI problems. Several hydroelastic cases, including those that have been very recently tested in the respective experimental facility, have been simulated. In general, it has been found that the flow damping effect is more pronounced in 3D, upon including the side walls as per the real physical model. For example, for the case of oil sloshing in a rolling tank, it has been found that the free surface predicted using the current 3D SPH-VCPM method is less violent (i.e., no unphysical wave breaking) than that of the 2D counterpart, which is tallied with the experimental observation. For the problem involving flow impact on a sluice gate in which the real experiment has been recently performed at Iskenderun Technical University, it has been found that the hydraulic jump phenomenon behind the sluice gate can be better reproduced using our current 3D FSI method as compared to the 2D FSI models. In general, the better prediction of free surface patterns has translated into more accurate estimation of free surface heights with respect to time at various locations.

From the simulation results, it is evident that the pressure field is not smooth near the boundary and the boundary layer thickens in a somewhat unphysical manner. This could be due to the artefact of the dynamic boundary condition (DBC) used for wall modeling. More accurate wall modeling techniques and associated analyses for FSI problems are hence necessary, without sacrificing the robustness of DBC. While the

VCPM particle simulation time per step reported in the current work is in the same order of magnitude as that of SPH (TLSPH particle simulation time per step is one order of magnitude larger than that of SPH (Zhan et al., 2019)) in the highly optimized DualSPHysics code, we believe that scalability of VCPM can be further improved by managing the shared and global memories more effectively. In fact, the real strength of VCPM method is its capability in modeling solid fracture. Some preliminary FSI results on the use of 3D SPH-VCPM method in modeling solid fracture have been shown in Appendix. Future works will include validation of this class of FSI problems involving solid fracture and implementation of more sophisticated bond-based failure criteria for studying real material fracture. One such interesting problem is the impact damage of laminate composites in the naval applications.

CRediT authorship contribution statement

K.C. Ng: Conceptualization, Methodology, Software, Validation, Formal analysis, Investigation, Resources, Data curation, Writing – original draft, Writing – review & editing, Visualization, Supervision, Project administration, Funding acquisition. **W.C. Low:** Writing – original draft, Visualization. **Hailong Chen:** Writing – review & editing, Software. **A. Tafuni:** Writing – review & editing, Software. **A. Nakayama:** Writing – review & editing.

Declaration of competing interest

The authors declare that they have no known competing financial interests or personal relationships that could have appeared to influence the work reported in this paper.

Data availability

Data will be made available on request.

Acknowledgement

The financial supports given by Ministry of Higher Education (MoHE), Malaysia under the Fundamental Research Grant Schemes: FRGS/1/2021/TK0/UNIM/02/6 and FRGS/1/2019/TK01/UTAR/01/1 are highly acknowledged.

Appendix

Collapse of a 3D solid structure – preliminary study

The inherent strength of lattice-spring model such as VCPM is its capability in modeling crack and fracture in a solid domain. Here, we intend to show some preliminary results of our 3D SPH-VCPM method in modeling crack in solid domain due to both actions of fluid force and solid body weight. The geometric details are shown in Fig. A1, where the solid structure consists of horizontal and vertical arms. A hydrostatic water column is located beside the vertical arm of the structure. The solid material considered is a brittle PMMA material with properties $E = 2.94$ GPa, $\nu^S = 0.38$, ultimate tensile strength $\sigma_T = 48$ MPa and $\rho^S = 1180$ kgm^{-3}. As shown in Fig. A1, there is an initial crack (represented using dark brown particles) near the bottom of the vertical arm which is supported on the ground. In the current simulation, the bond-based critical elongation failure criterion is adopted to model the cracking phenomenon in the solid structure. For this PMMA material, Chen and co-workers (Chen and Liu, 2016) have calibrated the following:

$$\Delta L^{crit} = \alpha(Dp) \tag{A1}$$

where Dp is the original bond length (initial particle spacing), ΔL^{crit} is the critical elongation of a spring bond, and α is the calibrated constant based on the material properties ($\alpha = 1.25\frac{Dp.\sigma_T}{2k}$). Here, k is the stiffness of the spring bond. Once the elongation of a spring bond exceeds ΔL^{crit}, the respective spring bond is broken, and force is no longer transmissible through the spring bond.

Fig. A2 shows the crack path of the PMMA structure as well as the speed of the SPH fluid particles as time elapses. It is interesting to note that the crack propagation in the solid structure is not started from the initial crack near the bottom of the vertical arm. Instead, as the extended horizontal arm (larger weight than the vertical arm) bends downward due to gravity, a new crack starts to form near the intersection between the horizontal and vertical arms and propagates thereafter (see Fig. A2 (c)). This new crack grows until the horizontal arm is completely detached from the vertical arm as shown in Fig. A2 (d). Soon after this complete detachment, the pre-existing crack near the bottom of the vertical arm starts to propagate as well as highlighted in Fig. A2 (e). In general, as the structure is collapsing, the fluid particles start to gain their momentums. As shown in Fig. A3, the fluid particles near the bottom start to enter the crack gap as it widens.

In the current preliminary simulation, the collision between those particles upon which the inter-connected bonds are broken is not considered. Future study will involve the implementations of suitable collision model to avoid the collision problem and other bond-based failure criteria.

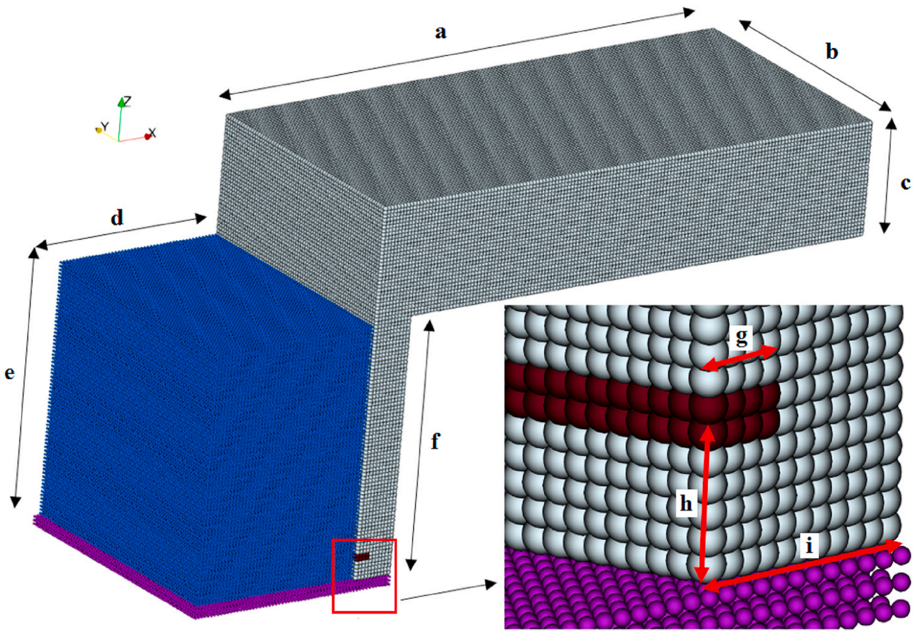

Fig. A1. Water column (blue particles) beside a PMMA structure (grey and dark brown particles) with crack near the bottom of the structure. Geometric information: $a = 151$ m; $b = 71$ m; $c = 31$ m; $d = 49$ m; $e = 69$ m; $f = 70$ m; $g = 4$ m; $h = 6$ m; and $i = 11$ m. The solid particles with disconnected bond in between (i.e. crack) are highlighted in dark brown colour. The ground is represented using purple particles.

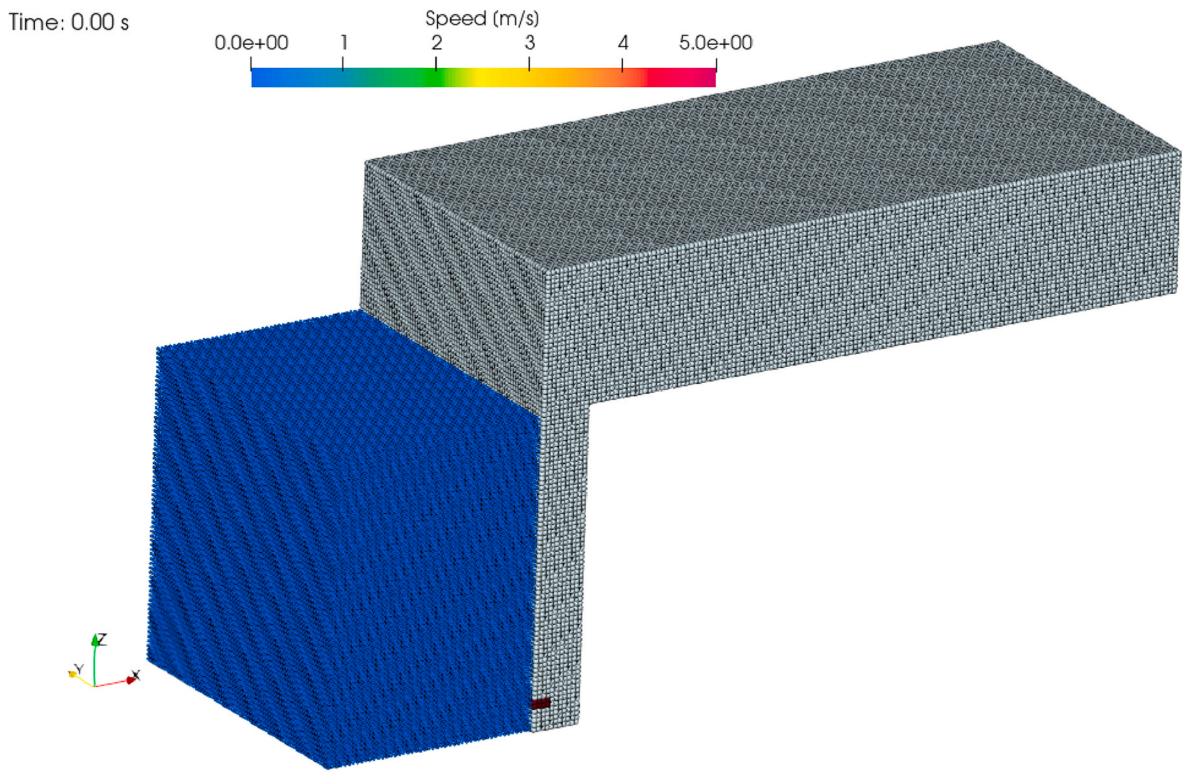

(a)

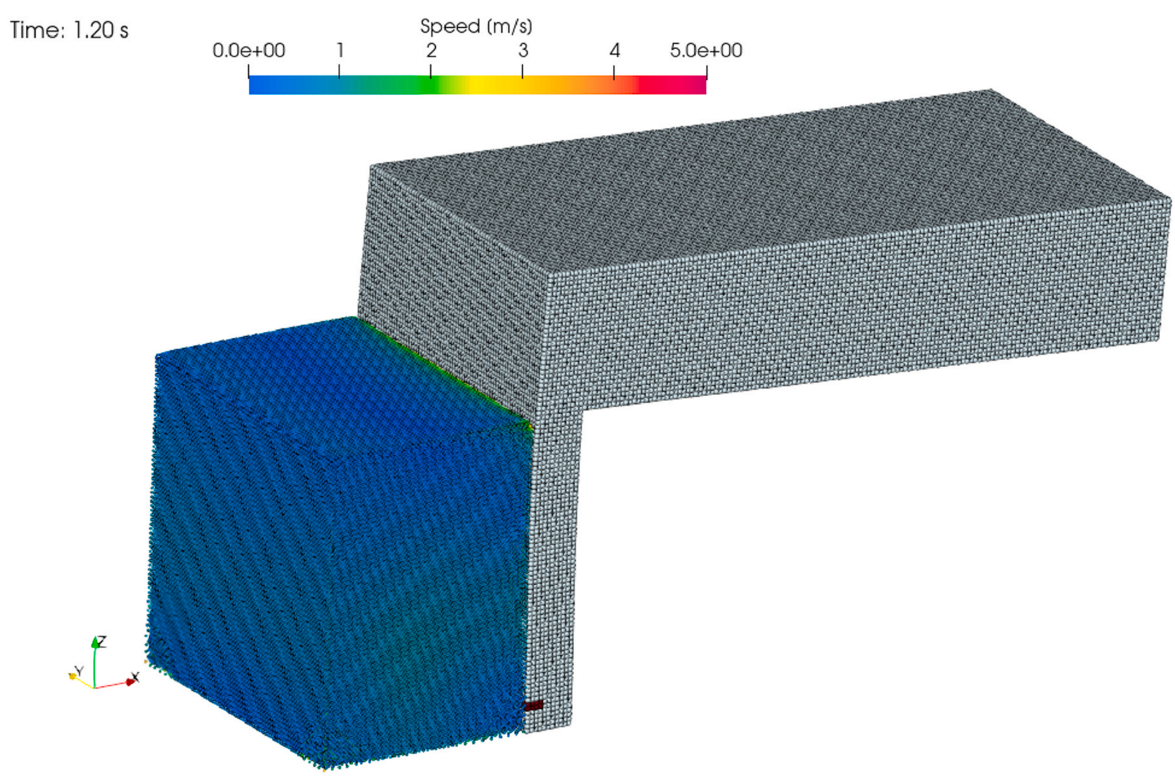

(b)

Fig. A2. The collapse of a solid structure and its interaction with neighbouring water particles coloured with speed values at different time frames: (a) $t = 0$ s; (b) $t = 1.20$ s; (c) $t = 1.58$ s; (d) $t = 1.70$ s; (e) $t = 2.00$ s and (f) $t = 2.96$ s. The solid particles with disconnected bond in between (i.e. crack) are highlighted in dark brown colour.

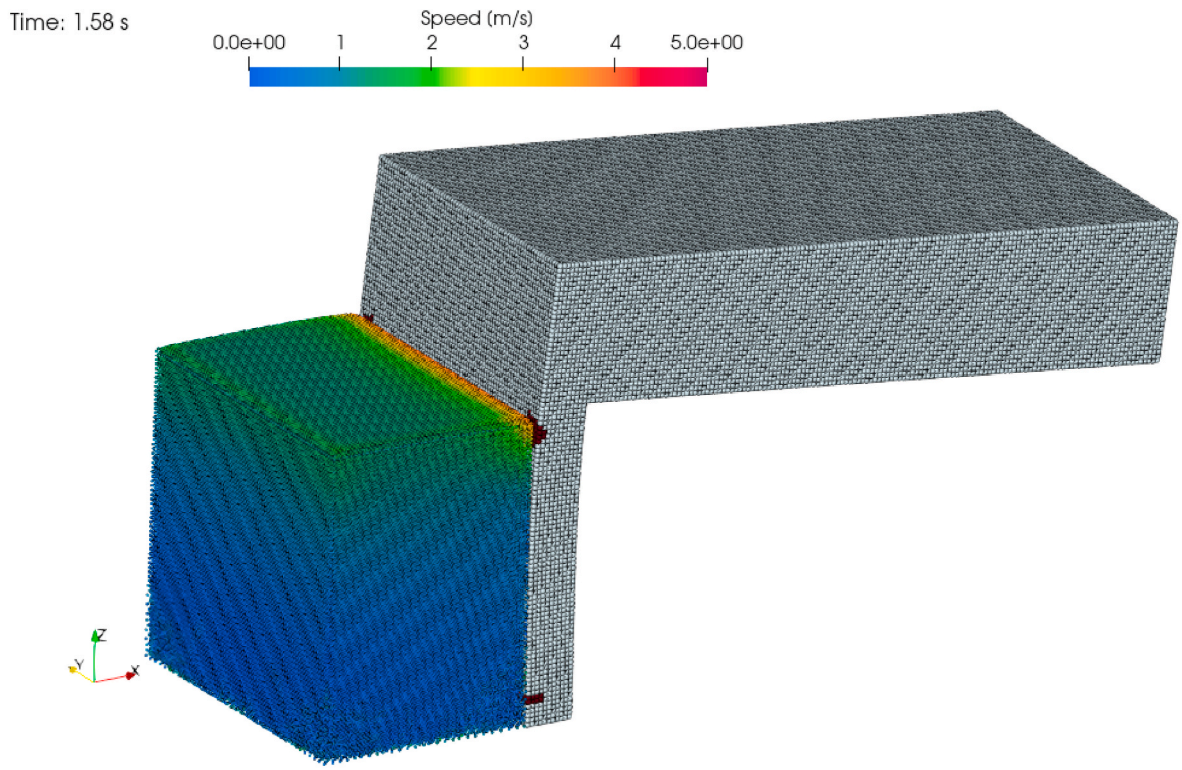

(c)

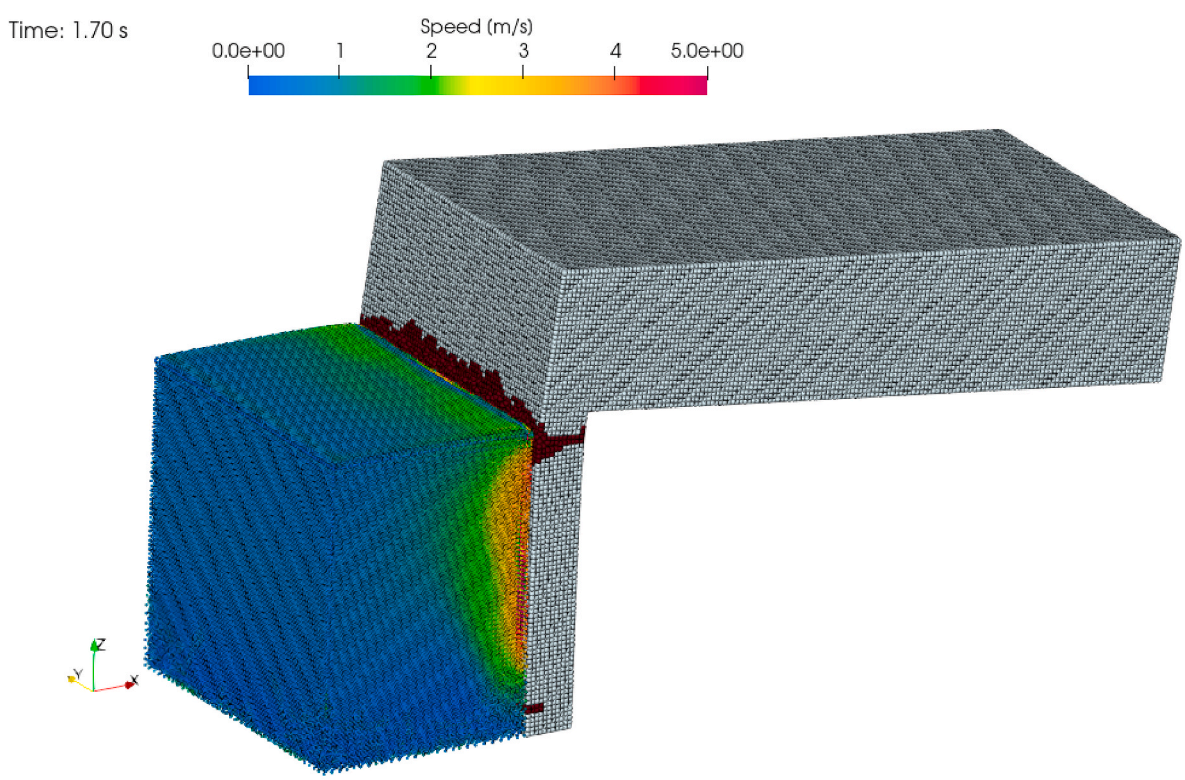

(d)

Fig. A2. (*continued*).

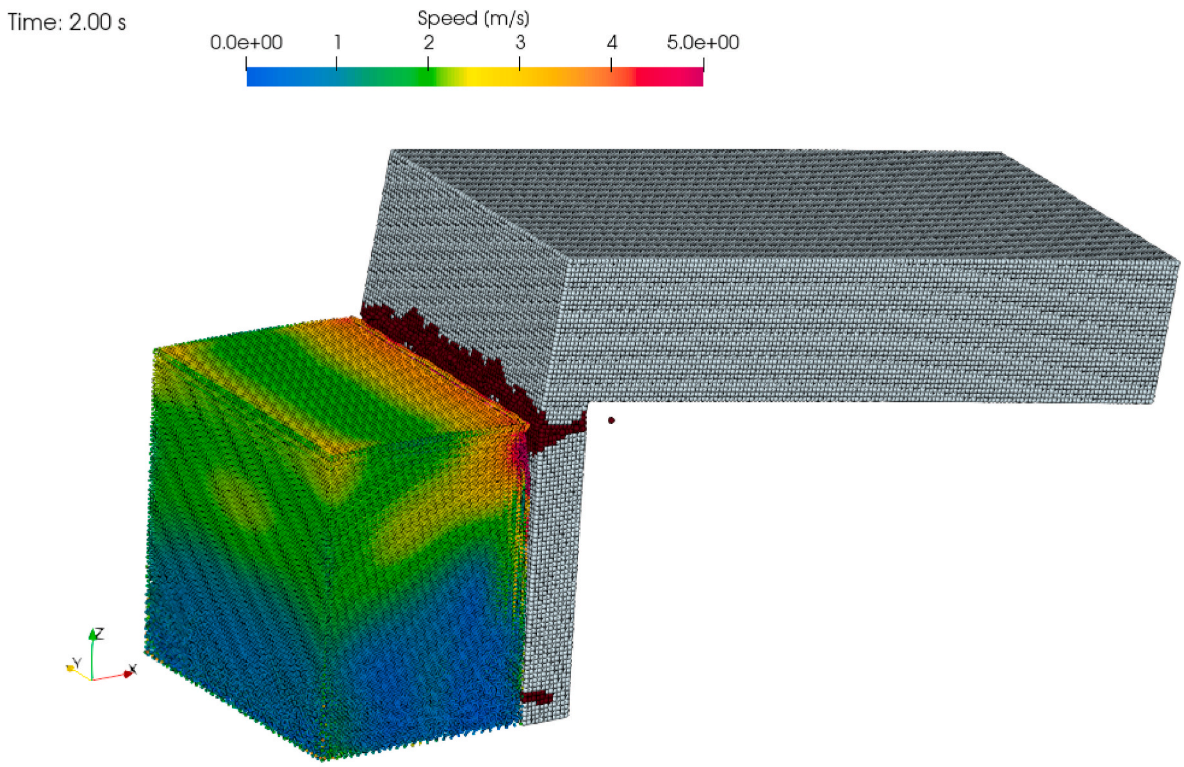

(e)

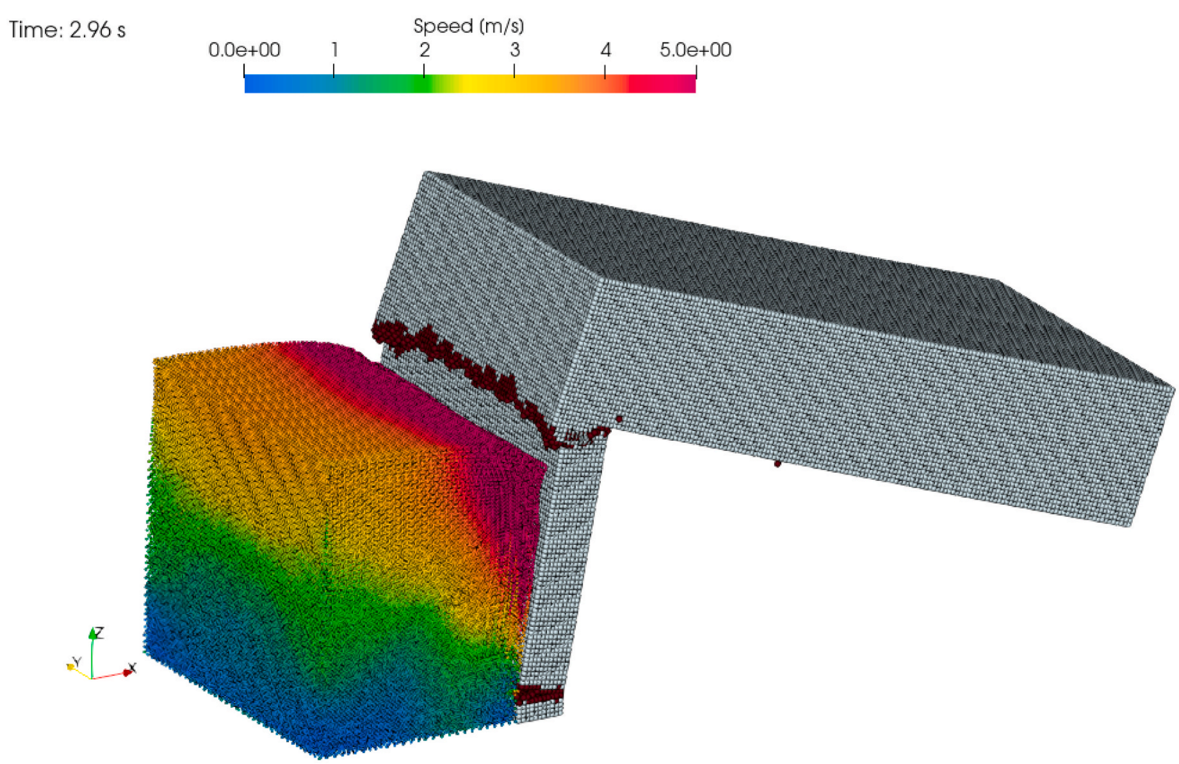

(f)

Fig. A2. (*continued*).

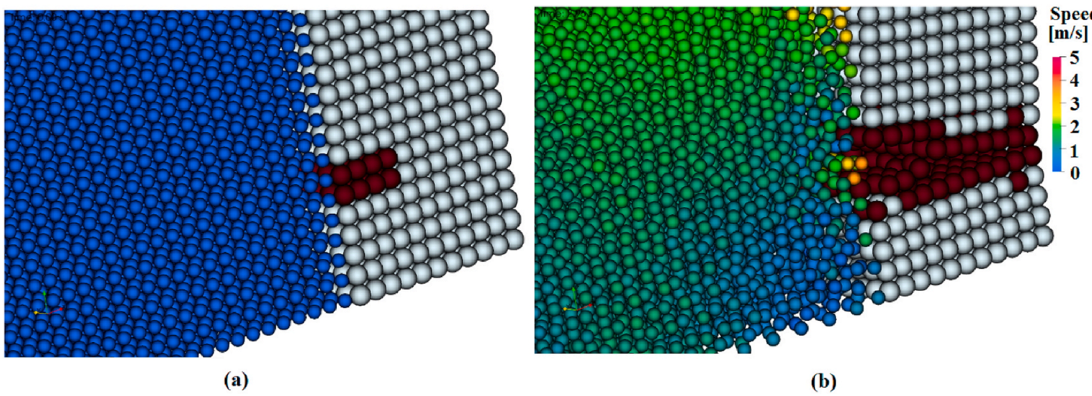

Fig. A3. Close-up views of particles near the crack at the bottom of the vertical arm at (a) $t = 0$ s and (b) $t = 2.96$ s. Water particles (coloured with speed values) start to move into the crack gap at $t = 2.96$ s as the gap widens. The solid particles with disconnected bond in between (i.e. crack) are highlighted in dark brown colour.

References

Adami, S., Hu, X.Y., Adams, N.A., 2012. A generalized wall boundary condition for smoothed particle hydrodynamics. J. Comput. Phys. 231, 7057–7075. https://doi.org/10.1016/j.jcp.2012.05.005.

Antoci, C., Gallati, M., Sibilla, S., 2007. Numerical simulation of fluid-structure interaction by SPH. Comput. Struct. 85, 879–890. https://doi.org/10.1016/j.compstruc.2007.01.002.

Antuono, M., Colagrossi, A., Marrone, S., 2012. Numerical diffusive terms in weakly-compressible SPH schemes. Comput. Phys. Commun. 183, 2570–2580. https://doi.org/10.1016/j.cpc.2012.07.006.

Ariane, M., Allouche, M.H., Bussone, M., Giacosa, F., Bernard, F., Barigou, M., et al., 2017. Discrete multi-physics: a mesh-free model of blood flow in flexible biological valve including solid aggregate formation. PLoS One 12, 1–15. https://doi.org/10.1371/journal.pone.0174795.

Belytschko, T., Guo, Y., Liu, W.K., Xiao, S.P., 2000. A unified stability analysis of meshless particle methods. Int. J. Numer. Methods Eng. 48, 1359–1400. https://doi.org/10.1002/1097-0207(20000730)48:9<1359::AID-NME829>3.0.CO;2-U.

Bonet, J., Lok, T.-S., 1999. Variational and momentum preservation aspects of smooth particle hydrodynamic formulations. Comput. Methods Appl. Mech. Eng. 180, 97–115.

Bouscasse, B., Antuono, M., Colagrossi, A., Lugni, C., 2013. Numerical and experimental investigation of nonlinear shallow water sloshing. Int. J. Nonlinear Sci. Numer. Stimul. 14, 123–138.

Chella, M.A., Tørum, A., Myrhaug, D., 2012. An overview of wave impact forces on offshore wind turbine substructures. Energy Proc. 20, 217–226. https://doi.org/10.1016/j.egypro.2012.03.022.

Chen, H., 2019. Constructing continuum-like measures based on a nonlocal lattice particle model: deformation gradient, strain and stress tensors. Int. J. Solid Struct. 169, 177–186. https://doi.org/10.1016/j.ijsolstr.2019.04.014.

Chen, J.K., Beraun, J.E., 2000. A generalized smoothed particle hydrodynamics method for nonlinear dynamic problems. Comput. Methods Appl. Mech. Eng. 190, 225–239. https://doi.org/10.1016/S0045-7825(99)00422-3.

Chen, H., Liu, Y., 2016. A non-local 3D lattice particle framework for elastic solids. Int. J. Solid Struct. 81, 411–420. https://doi.org/10.1016/j.ijsolstr.2015.12.026.

Chen, H., Lin, E., Liu, Y., 2014. A novel Volume-Compensated Particle method for 2D elasticity and plasticity analysis. Int. J. Solid Struct. 51, 1819–1833. https://doi.org/10.1016/j.ijsolstr.2014.01.025.

Crespo, A.J.C., Gómez-Gesteira, M., Dalrymple, R.A., 2007. Boundary conditions generated by dynamic particles in SPH methods. Comput. Mater. Continua (CMC). https://doi.org/10.3970/cmc.2007.005.173.

Crespo, A.J.C., Dom\'\inguez, J.M., Rogers, B.D., Gómez-Gesteira, M., Longshaw, S., Canelas, R., et al., 2015. DualSPHysics: open-source parallel CFD solver based on smoothed particle hydrodynamics (SPH). Comput. Phys. Commun. 187, 204–216.

Dalrymple, R.A., Rogers, B.D., 2006. Numerical modeling of water waves with the SPH method. Coast. Eng. 53, 141–147.

Danielsen, F., Sørensen, M.K., Olwig, M.F., Selvam, V., Parish, F., Burgess, N.D., et al., 2005. The Asian tsunami: a protective role for coastal vegetation. Science (80-) 310, 643. https://doi.org/10.1126/science.1118387.

English, A., Domínguez, J.M., Vacondio, R., Crespo, A.J.C., Stansby, P.K., Lind, S.J., et al., 2021. Modified dynamic boundary conditions (mDBC) for general-purpose smoothed particle hydrodynamics (SPH): application to tank sloshing, dam break and fish pass problems. Comput. Times Part Mech. https://doi.org/10.1007/s40571-021-00403-3.

Fourey, G., Hermange, C., Le Touzé, D., Oger, G., 2017. An efficient FSI coupling strategy between smoothed particle hydrodynamics and finite element methods. Comput. Phys. Commun. 217, 66–81. https://doi.org/10.1016/j.cpc.2017.04.005.

Fourtakas, G., Dominguez, J.M., Vacondio, R., Rogers, B.D., 2019. Local uniform stencil (LUST) boundary condition for arbitrary 3-D boundaries in parallel smoothed particle hydrodynamics (SPH) models. Comput. Fluids 190, 346–361. https://doi.org/10.1016/j.compfluid.2019.06.009.

Ganzenmüller, G.C., 2015. An hourglass control algorithm for Lagrangian Smooth Particle Hydrodynamics. Comput. Methods Appl. Mech. Eng. 286, 87–106. https://doi.org/10.1016/j.cma.2014.12.005.

Goodier, J.N., Timoshenko, S., 1970. Theory of Elasticity. McGraw-Hill.

Gotoh, H., Khayyer, A., Shimizu, Y., 2021. Entirely Lagrangian meshfree computational methods for hydroelastic fluid-structure interactions in ocean engineering—reliability, adaptivity and generality. Appl. Ocean Res. 115, 102822 https://doi.org/10.1016/j.apor.2021.102822.

Gray, J.P., Monaghan, J.J., Swift, R.P., 2001. SPH elastic dynamics. Comput. Methods Appl. Mech. Eng. 190, 6641–6662. https://doi.org/10.1016/S0045-7825(01)00254-7.

Hermange, C., Oger, G., Le Chenadec, Y., Le Touzé, D., 2019. A 3D SPH–FE coupling for FSI problems and its application to tire hydroplaning simulations on rough ground. Comput. Methods Appl. Mech. Eng. 355, 558–590. https://doi.org/10.1016/j.cma.2019.06.033.

Hirt, C.W., Nichols, B.D., 1981. Volume of fluid (VOF) method for the dynamics of free boundaries. J. Comput. Phys. 39, 201–225. https://doi.org/10.1016/0021-9991(81)90145-5.

Idelsohn, S.R., Marti, J., Souto-Iglesias, A., Oñate, E., 2008. Interaction between an elastic structure and free-surface flows: experimental versus numerical comparisons using the PFEM. Comput. Mech. 43, 125–132. https://doi.org/10.1007/s00466-008-0245-7.

Khayyer, A., Gotoh, H., Falahaty, H., Shimizu, Y., 2018. Towards development of enhanced fully-Lagrangian mesh-free computational methods for fluid-structure interaction. J. Hydrodyn. 30, 49–61.

Khayyer, A., Shimizu, Y., Gotoh, H., Hattori, S., 2021. Multi-resolution ISPH-SPH for accurate and efficient simulation of hydroelastic fluid-structure interactions in ocean engineering. Ocean Eng. 226, 108652 https://doi.org/10.1016/j.oceaneng.2021.108652.

Leimkuhler, B.J., Reich, S., Skeel, R.D., 1996. Integration methods for molecular dynamics. In: Mesirov, J.P., Schulten, K., Sumners, D.W. (Eds.), Math. Approaches to Biomol. Struct. Dyn. Springer New York, New York, NY, pp. 161–185. https://doi.org/10.1007/978-1-4612-4066-2_10.

Liu, M.B., Liu, G.R., 2006. Restoring particle consistency in smoothed particle hydrodynamics. Appl. Numer. Math. 56, 19–36. https://doi.org/10.1016/j.apnum.2005.02.012.

Ming, F.R., Zhang, A.M., Cheng, H., Sun, P.N., 2018. Numerical simulation of a damaged ship cabin flooding in transversal waves with Smoothed Particle Hydrodynamics method. Ocean Eng. 165, 336–352. https://doi.org/10.1016/j.oceaneng.2018.07.048.

Monaghan, J.J., 1994. Simulating free surface flows with SPH. J. Comput. Phys. 110, 399–406. https://doi.org/10.1006/jcph.1994.1034.

Nasar, A.M.A., Rogers, B.D., Revell, A., Stansby, P.K., 2019. Flexible slender body fluid interaction: vector-based discrete element method with Eulerian smoothed particle hydrodynamics. Comput \& Fluids 179, 563–578.

Ng, K.C., Alexiadis, A., Chen, H., Sheu, T.W.H., 2020. A coupled smoothed particle hydrodynamics-volume compensated particle method (SPH-VCPM) for fluid structure interaction (FSI) modelling. Ocean Eng 218. https://doi.org/10.1016/j.oceaneng.2020.107923.

Ng, K.C., Alexiadis, A., Chen, H., Sheu, T.W.H., 2021. Numerical computation of fluid–solid mixture flow using the SPH–VCPM–DEM method. J Fluids Struct 106. https://doi.org/10.1016/j.jfluidstructs.2021.103369.

Ng, K.C., Alexiadis, A., Ng, Y.L., 2022. An improved particle method for simulating Fluid-Structure Interactions: the multi-resolution SPH-VCPM approach. Ocean Eng 247. https://doi.org/10.1016/j.oceaneng.2022.110779.

O'Connor, J., Rogers, B.D., 2021. A fluid–structure interaction model for free-surface flows and flexible structures using smoothed particle hydrodynamics on a GPU. J Fluids Struct 104, 103312. https://doi.org/10.1016/j.jfluidstructs.2021.103312.

Paik, K.J., Carrica, P.M., 2014. Fluid-structure interaction for an elastic structure interacting with free surface in a rolling tank. Ocean Eng 84, 201–212. https://doi.org/10.1016/j.oceaneng.2014.04.016.
Souto-Iglesias, A., Idelsohn, S.R., Marti, J., Zamora-Rodríguez, R., Oñate, E., 2008. Modeling of Free Surface Flows with Elastic Bodies Interactions, 27th Symp. Nav. Hydrodyn., Seoul, Korea, 5-10 October 2008.
Sun, P.N., Le Touzé, D., Oger, G., Zhang, A.M., 2021. An accurate FSI-SPH modeling of challenging fluid-structure interaction problems in two and three dimensions. Ocean Eng 221. https://doi.org/10.1016/j.oceaneng.2020.108552.
Sussman, M., 1994. A level set approach for computing solutions to incompressible two-phase flow. J Comput Phys 114, 146–159. https://doi.org/10.1006/jcph.1994.1155.
Swelge, J.W., Hicks, D.L., Attaway, S.W., 1995. SPH stability Analysis.pdf. J Comput Phys 116, 123–134.
Tang, Y., Jiang, Q., Zhou, C., 2018. A Lagrangian-based SPH-DEM model for fluid–solid interaction with free surface flow in two dimensions. Appl Math Model 62, 436–460. https://doi.org/10.1016/j.apm.2018.06.013.
Vignjevic, R., Campbell, J., Libersky, L., 2000. A treatment of zero-energy modes in the smoothed particle hydrodynamics method. Comput Methods Appl Mech Eng 184, 67–85. https://doi.org/10.1016/S0045-7825(99)00441-7.
Wang, M., Avital, E.J., Bai, X., Ji, C., Xu, D., Williams, J.J.R., et al., 2020. Fluid–structure interaction of flexible submerged vegetation stems and kinetic turbine blades. Comput Part Mech 7, 839–848. https://doi.org/10.1007/s40571-019-00304-6.
Wendland, H., 1995. Piecewise polynomial, positive definite and compactly supported radial functions of minimal degree. Adv Comput Math 4, 389–396.
Wu, K., Yang, D., Wright, N., 2016. A coupled SPH-DEM model for fluid-structure interaction problems with free-surface flow and structural failure. Comput Struct 177, 141–161. https://doi.org/10.1016/j.compstruc.2016.08.012.
Yang, Q., Jones, V., McCue, L., 2012. Free-surface flow interactions with deformable structures using an SPH-FEM model. Ocean Eng 55, 136–147. https://doi.org/10.1016/j.oceaneng.2012.06.031.
Yilmaz, A., Kocaman, S., Demirci, M., 2021. Numerical modeling of the dam-break wave impact on elastic sluice gate: a new benchmark case for hydroelasticity problems. Ocean Eng 231, 108870. https://doi.org/10.1016/j.oceaneng.2021.108870.
Yilmaz, A., Kocaman, S., Demirci, M., 2022. Numerical analysis of hydroelasticity problems by coupling WCSPH with multibody dynamics. Ocean Eng 243, 110205. https://doi.org/10.1016/j.oceaneng.2021.110205.
Zhan, L., Peng, C., Zhang, B., Wu, W., 2019. A stabilized TL–WC SPH approach with GPU acceleration for three-dimensional fluid–structure interaction. J Fluids Struct 86, 329–353. https://doi.org/10.1016/j.jfluidstructs.2019.02.002.
Zhang, C., Rezavand, M., Hu, X., 2021. A multi-resolution SPH method for fluid-structure interactions. J Comput Phys 429, 110028. https://doi.org/10.1016/j.jcp.2020.110028.